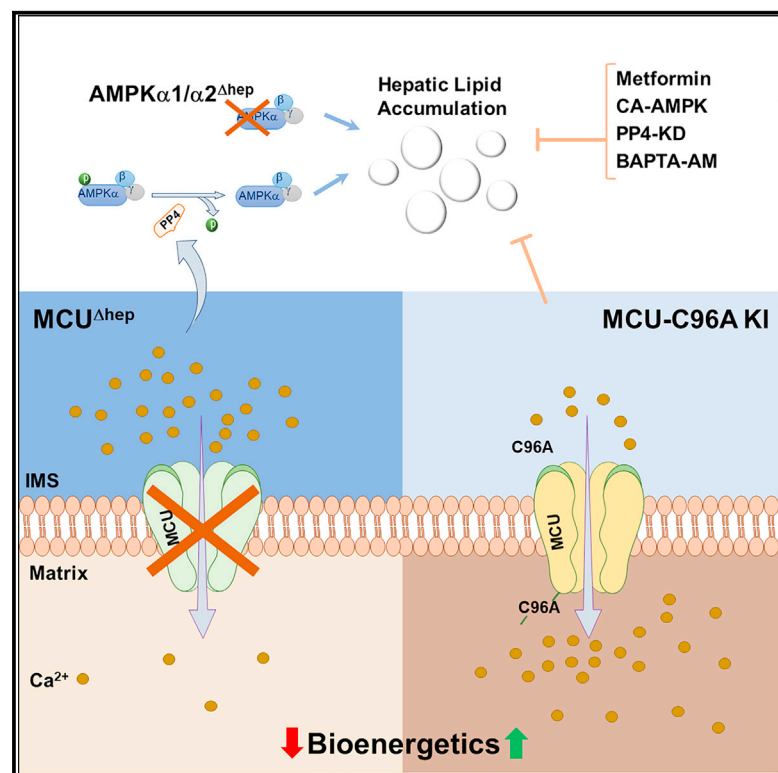**Article**

Blockade of MCU-Mediated Ca^{2+} Uptake Perturbs Lipid Metabolism via PP4-Dependent AMPK Dephosphorylation

Graphical Abstract

Authors

Dhanendra Tomar, Fabián Jaña, Zhiwei Dong, ..., Rexford S. Ahima, Joseph A. Baur, Muniswamy Madesh

Correspondence

muniswamy@uthscsa.edu

In Brief

Hepatic mitochondrial Ca^{2+} shapes bioenergetics and lipid homeostasis. Tomar et al. demonstrate that MCU-mediated $_c$Ca^{2+} buffering serves as a crucial step in controlling hepatic fuel metabolism through an MCU/PP4/AMPK molecular cascade. Identification of these molecular signaling events aids in understanding how perturbation of mitochondrial ion homeostasis may contribute to the etiology of metabolic disorders.

Highlights

- Mitochondrial Ca^{2+} powers FAO-dependent hepatocyte mitochondrial respiration

- Hepatic MCU deletion promotes lipid accumulation and lowers ketone bodies

- Blockade of $_m$Ca^{2+} buffering enhances AMPK dephosphorylation through PP4

- Restoration of AMPK activity in MCU$^{\Delta hep}$ model improves lipid clearance

CellPress

Blockade of MCU-Mediated Ca^{2+} Uptake Perturbs Lipid Metabolism via PP4-Dependent AMPK Dephosphorylation

Dhanendra Tomar,[1,2] Fabián Jaña,[1,2] Zhiwei Dong,[1,2] William J. Quinn III,[3] Pooja Jadiya,[2] Sarah L. Breves,[1,2]
Cassidy C. Daw,[4] Subramanya Srikantan,[4] Santhanam Shanmughapriya,[1,2] Neeharika Nemani,[1,2] Edmund Carvalho,[1,2]
Aparna Tripathi,[1,2] Alison M. Worth,[1,2] Xueqian Zhang,[2] Roshanak Razmpour,[5] Ajay Seelam,[1,2] Stephen Rhode,[1,2]
Anuj V. Mehta,[2,6] Michael Murray,[1,2] Daniel Slade,[1,2] Servio H. Ramirez,[5] Prashant Mishra,[7] Glenn S. Gerhard,[1]
Jeffrey Caplan,[8] Luke Norton,[9] Kumar Sharma,[4] Sudarsan Rajan,[1,2] Darius Balciunas,[6] Dayanjan S. Wijesinghe,[10]
Rexford S. Ahima,[11] Joseph A. Baur,[3] and Muniswamy Madesh[1,2,4,12,*]

[1]Department of Medical Genetics and Molecular Biochemistry, Lewis Katz School of Medicine at Temple University, Philadelphia,
PA 19140, USA
[2]Center for Translational Medicine, Lewis Katz School of Medicine at Temple University, Philadelphia, PA 19140, USA
[3]Department of Physiology and Institute for Diabetes, Obesity, and Metabolism, Perelman School of Medicine, University of Pennsylvania,
Philadelphia, PA 19104, USA
[4]Department of Medicine and Nephrology, Center for Precision Medicine, University of Texas Health San Antonio, San Antonio,
TX 78229, USA
[5]Department of Pathology and Laboratory Medicine, Lewis Katz School of Medicine at Temple University, Philadelphia, PA 19140, USA
[6]Department of Biology, Temple University, Philadelphia, PA 19122, USA
[7]Children's Medical Center Research Institute, University of Texas Southwestern Medical Center, Dallas, TX 75390, USA
[8]Department of Biological Sciences, Delaware Biotechnology Institute, University of Delaware, Newark, DE 19711, USA
[9]Diabetes Division, University of Texas Health Science Center, San Antonio, TX, USA
[10]Department of Surgery, Virginia Commonwealth University, Richmond, VA 23298, USA
[11]Division of Endocrinology, Diabetes and Metabolism, John Hopkins University School of Medicine, Baltimore, MD 21287, USA
[12]Lead Contact
*Correspondence: muniswamy@uthscsa.edu
https://doi.org/10.1016/j.celrep.2019.02.107

SUMMARY

Mitochondrial Ca^{2+} uniporter (MCU)-mediated Ca^{2+} uptake promotes the buildup of reducing equivalents that fuel oxidative phosphorylation for cellular metabolism. Although MCU modulates mitochondrial bioenergetics, its function in energy homeostasis *in vivo* remains elusive. Here we demonstrate that deletion of the *Mcu* gene in mouse liver (MCU$^{\Delta hep}$) and in *Danio rerio* by CRISPR/Cas9 inhibits mitochondrial Ca^{2+} (mCa^{2+}) uptake, delays cytosolic Ca^{2+} (cCa^{2+}) clearance, reduces oxidative phosphorylation, and leads to increased lipid accumulation. Elevated hepatic lipids in MCU$^{\Delta hep}$ were a direct result of extramitochondrial Ca^{2+}-dependent protein phosphatase-4 (PP4) activity, which dephosphorylates AMPK. Loss of AMPK recapitulates hepatic lipid accumulation without changes in MCU-mediated Ca^{2+} uptake. Furthermore, reconstitution of active AMPK, or PP4 knockdown, enhances lipid clearance in MCU$^{\Delta hep}$ hepatocytes. Conversely, gain-of-function MCU promotes rapid mCa^{2+} uptake, decreases PP4 levels, and reduces hepatic lipid accumulation. Thus, our work uncovers an MCU/PP4/AMPK molecular cascade that links Ca^{2+} dynamics to hepatic lipid metabolism.

INTRODUCTION

Mitochondrial Ca^{2+} (mCa^{2+}) uptake plays a fundamental role in the spatiotemporal regulation of cytosolic Ca^{2+} (cCa^{2+}) and cellular bioenergetics in most cell types (Balaban, 2009; Baughman et al., 2011; Cárdenas et al., 2010; De Stefani et al., 2011; Denton and McCormack, 1980; Drago et al., 2011; Hajnóczky et al., 2000; Mallilankaraman et al., 2012a, 2012b). Because of the highly selective permeability of the inner mitochondrial membrane (IMM), mCa^{2+} uptake is tightly regulated by the mitochondrial electrochemical gradient ($\Delta\Psi_m$), generated by the electron transport chain and facilitated by the mitochondrial Ca^{2+} uniporter (MCU) complex (Baughman et al., 2011; De Stefani et al., 2011; Kirichok et al., 2004). The core component of the complex, the MCU, and its regulators MICU1, MICU2, MCUR1, essential MCU regulator (EMRE), and MCUb have been identified and actively studied in recent years (Baughman et al., 2011; De Stefani et al., 2011, 2016; Kamer and Mootha, 2014; Mallilankaraman et al., 2012a, 2012b; Patron et al., 2014; Payne et al., 2017; Perocchi et al., 2010; Plovanich et al., 2013; Raffaello et al., 2013; Sancak et al., 2013; Tomar et al., 2016). The MCU-regulated mCa^{2+} fine-tunes mitochondrial bioenergetics through activation of Ca^{2+}-dependent dehydrogenases and promotion of ATP synthesis (Balaban, 2009; Glancy and Balaban, 2012; Glancy et al., 2013). However, MCU-mediated mCa^{2+} overload favors opening of the mitochondrial permeability transition pore (mPTP), leading to a cascade of cell death events (Bernardi, 1999; Biasutto et al., 2016; Izzo et al., 2016; Shanmughapriya
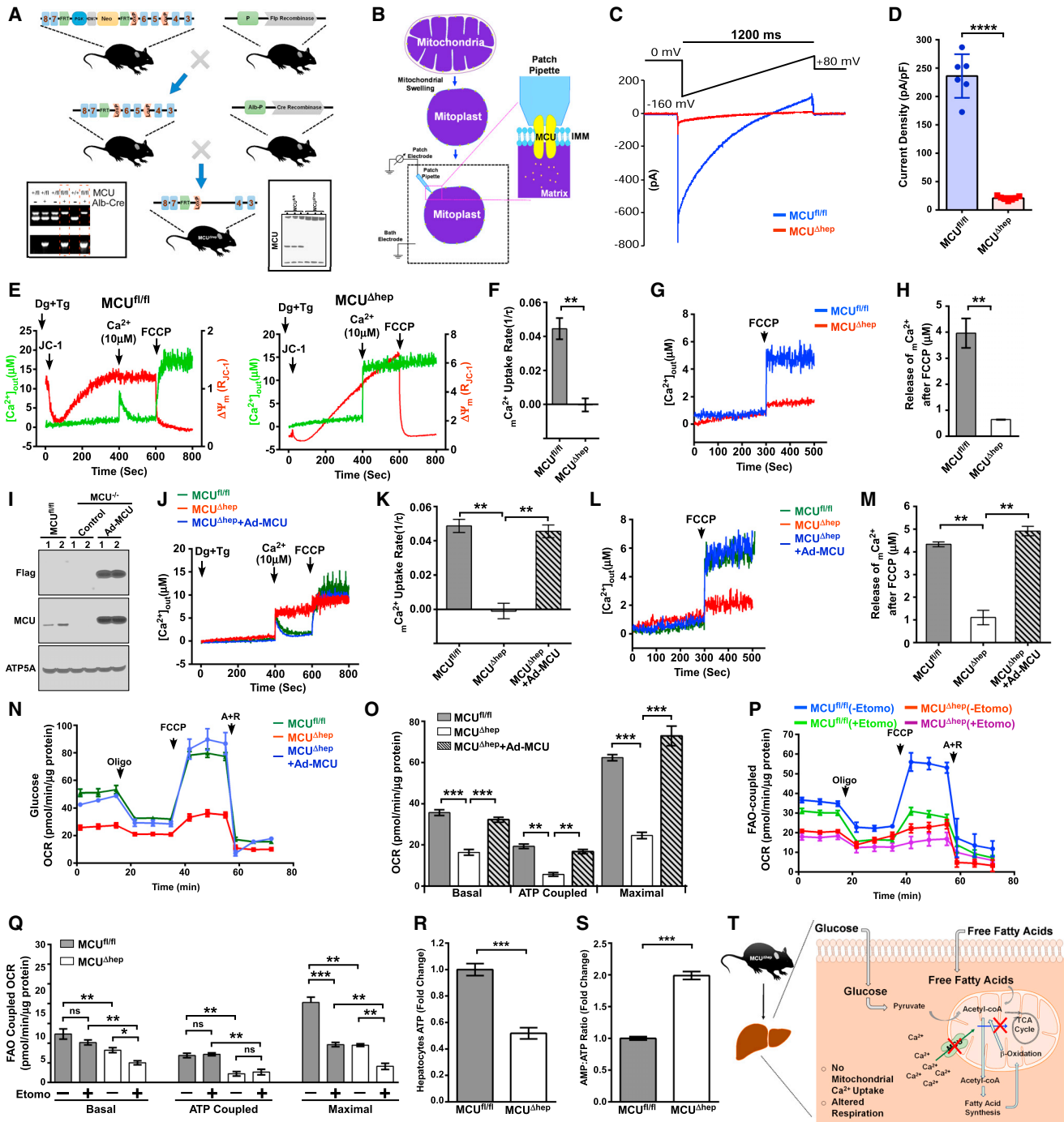
Figure 1. Hepatocyte MCU Activity Regulates FAO-Coupled Mitochondrial Respiration

(A) Generation and confirmation of MCU$^{\Delta hep}$ mice by PCR genotyping (left) and western blotting (right).

(B) Schematic representation of the patch-clamp technique for measuring MCU channel activity.

(C) Representative I_{MCU} traces derived from MCU$^{fl/fl}$ and MCU$^{\Delta hep}$ mitoplasts.

(D) I_{MCU} densities (picoamperes/picofarads) in mitoplasts. n = 6.

(E) Representative traces of extramitochondrial Ca^{2+} ([Ca^{2+}]$_{out}$) clearance and $\Delta\Psi$m in permeabilized hepatocytes from MCU$^{fl/fl}$ and MCU$^{\Delta hep}$. n = 3.

(F) $_m$Ca^{2+} uptake rate calculated from (E). n = 3.

(G) Representative traces of [Ca^{2+}]$_{out}$ rise from MCU$^{fl/fl}$ and MCU$^{\Delta hep}$. n = 3.

(H) Quantification of $_m$Ca^{2+} after addition of carbonyl cyanide 4-(trifluoromethoxy)phenylhydrazone (FCCP) from (G). n = 3.

(I) Immunoblot for the reconstitution of MCU in MCU$^{\Delta hep}$ mice using adenovirus-mediated delivery. n = 2.

(legend continued on next page)

et al., 2015a). Despite evidence that MCU functions as a multi-faceted oligomeric complex, the molecular mechanisms underlying the requirement of this complex for cellular metabolism *in vivo* remain highly debated (Kwong et al., 2015; Liu et al., 2017; Luongo et al., 2015; Pan et al., 2013; Tomar et al., 2016).

The liver plays a central role in carbohydrate and lipid metabolism, and metabolic dysfunction in this organ has a significant effect on whole-body energy homeostasis. An imbalance between lipid catabolism and anabolism, resulting in hepatic lipid accumulation, is observed in several metabolic disorders, including diabetes, obesity, and nonalcoholic fatty liver disease (Fu et al., 2011; Mayes and Felts, 1967; Perry et al., 2014; van den Berghe, 1991). Mitochondria comprise around 18% of the hepatocyte volume and form a very efficient $_cCa^{2+}$ regulatory system in hepatocytes (Weibel et al., 1969). Hepatic mitochondria have a high Ca^{2+} threshold for the opening of MCU channels and are directly coupled to oxidative phosphorylation (OXPHOS) (Paillard et al., 2017). Therefore, in hepatic tissue, $_mCa^{2+}$ may play a critical role in shaping metabolic outcomes. However, the mechanistic link between Ca^{2+} dynamics and lipid metabolism, if any, remains unknown.

Because the MCU is the primary driver of changes in $_mCa^{2+}$ and is responsible for Ca^{2+}-induced remodeling of mitochondrial function, we generated loss- and gain-of-function mouse models for this protein. Genetic ablation of *Mcu* from hepatocytes results in depletion of matrix Ca^{2+} and impaired OXPHOS activity. Hepatic lipid accumulation occurs as a result of delayed $_cCa^{2+}$ clearance and protein phosphatase 4-dependent AMP-activated protein kinase (AMPK) dephosphorylation. In parallel, acute deletion of hepatic AMPKα1α2 isoforms was sufficient to raise hepatic triglyceride levels, supporting a model where impaired AMPK activity is the mechanistic link between $_mCa^{2+}$ buffering and steatosis. Importantly, $_cCa^{2+}$ chelation or metformin treatment restored AMPK phosphorylation and lipid clearance in MCU$^{\Delta hep}$ hepatocytes. These results demonstrate that MCU-mediated $_cCa^{2+}$ buffering serves as a crucial step in controlling hepatic fuel metabolism.

RESULTS

Loss of *Mcu* Lowers Fatty Acid Oxidation-Coupled Mitochondrial Oxygen Consumption in Hepatocytes

To decipher the role of $_mCa^{2+}$ in liver metabolism, we generated a liver-specific knockout mouse model of *Mcu* (MCU$^{fl/fl}$Alb-Cre$^+$; hereafter referred to as MCU$^{\Delta hep}$) by crossing the MCU$^{fl/fl}$ C57BL/6 mouse with the hepatocyte-specific Cre-recombinase line (Figures 1A and S1A). MCU$^{\Delta hep}$ mitochondria showed a striking deficit in their MCU current (I_{MCU}), which further establishes that MCU is the core component of the uniporter complex necessary for hepatic $_mCa^{2+}$ uptake (Figures 1B–1D). Consistently, permeabilized hepatocytes from MCU$^{fl/fl}$ but not MCU$^{\Delta hep}$ exposed to a bolus of 10 μM Ca^{2+} exhibited rapid $_mCa^{2+}$ uptake (Figures 1E and 1F) without any effect on $\Delta\Psi_m$ (Figures 1E, S1B, and S1C). Although mitochondria are known to sequester inositol 1,4,5-trisphosphate receptor (IP$_3$R) and calcium-release activated channel (CRAC)-mediated $_cCa^{2+}$ (Cárdenas et al., 2010; Gilabert and Parekh, 2000; Hajnóczky et al., 1999, 2000; Hawkins et al., 2010; Pacher et al., 2000), it was unknown whether the basal mitochondrial matrix Ca^{2+} is altered in MCU$^{\Delta hep}$ mitochondria. Using permeabilized primary hepatocytes (Mallilankaraman et al., 2012a, 2012b; Shanmughapriya et al., 2015b; Tomar et al., 2016), we found that MCU$^{\Delta hep}$ hepatocytes have ~0.5 μM mitochondrial matrix calcium, which is ~8-fold less than Mcu$^{fl/fl}$ hepatocytes (~4.0 μM) (Figures 1G and 1H). To further validate the specificity of *Mcu* loss in MCU$^{\Delta hep}$ mice, we reconstituted the FLAG-tagged MCU wild-type (WT) in MCU$^{\Delta hep}$ mice through adenoviral delivery (Figure 1I). The adenoviral expression of MCU-FLAG restored both MCU-mediated $_mCa^{2+}$ uptake and basal matrix Ca^{2+} (Figures 1J–1M). We next sought to determine whether deletion of MCU lowers mitochondrial reactive oxygen species (mROS) production in hepatocytes. Primary hepatocytes isolated from MCU$^{fl/fl}$ and MCU$^{\Delta hep}$ mice were incubated with MitoSOX Red to visualize mROS levels, and basal mROS is greatly suppressed in MCU$^{\Delta hep}$ (Figures S1D and S1E), indicating a role for MCU-dependent $_mCa^{2+}$ uptake in mROS production.

Next, we found no changes in OXPHOS protein complex expression (Figure S1H), despite a greatly diminished basal mitochondrial oxygen consumption rate (OCR) in MCU$^{\Delta hep}$ hepatocytes (Figures S1F and 1G). Maximal uncoupled and ATP-coupled OCRs were also found to be significantly decreased (Figures S1F and 1G), suggesting a lack of optimal production of Ca^{2+}-dependent reducing equivalents like nicotinamide adenine dinucleotide (NADH) in the matrix (Glancy and Balaban, 2012; Glancy et al., 2013; White et al., 2005). Adenoviral reconstitution of MCU-FLAG in MCU$^{\Delta hep}$ mice restored the basal, maximal, and ATP-coupled OCRs in primary hepatocytes (Figures 1N and 1O). Because $_mCa^{2+}$ occupies a central role in mitochondrial bioenergetics, and alterations in MCU-mediated $_mCa^{2+}$ uptake may account for the differences observed in glucose and fat oxidation, we speculated that the fatty acid oxidation (FAO)-coupled OCR was compromised in MCU$^{\Delta hep}$ hepatocytes. To examine the FAO-dependent OCR,

(J) Reconstitution of MCU restores [Ca^{2+}]$_{out}$ clearance ability. n = 4.
(K) $_mCa^{2+}$ uptake rate calculated from (J). n = 4.
(L) MCU reconstitution restores the matrix Ca^{2+} in MCU$^{\Delta hep}$. Shown are representative traces of [Ca^{2+}]$_{out}$ rise in response to FCCP. n = 4.
(M) Quantification of $_mCa^{2+}$ calculated after addition of FCCP from (L). n = 4.
(N) MCU reconstitution restores the OCR in MCU KO hepatocytes. n = 3.
(O) Quantification of basal, ATP-coupled, and maximal OCRs in hepatocytes from (N). n = 3.
(P) The FAO OCR was measured in MCU$^{fl/fl}$ and MCU$^{\Delta hep}$ hepatocytes using palmitate as a substrate with or without etomoxir (40 μM). n = 3.
(Q) Quantification of basal, ATP-coupled, and maximal FAO-coupled OCRs from (P). n = 3.
(R) Measurement of hepatocyte ATP. n = 3.
(S) Measurement of AMP:ATP ratio in hepatocytes. n = 3. Statistical analysis: mean ± SEM. *p < 0.05, **p < 0.01, ***p < 0.001; ns, non-significant.
(T) Schematic of hepatocyte deletion of MCU, showing reduction in $_mCa^{2+}$ and bioenergetic parameters.
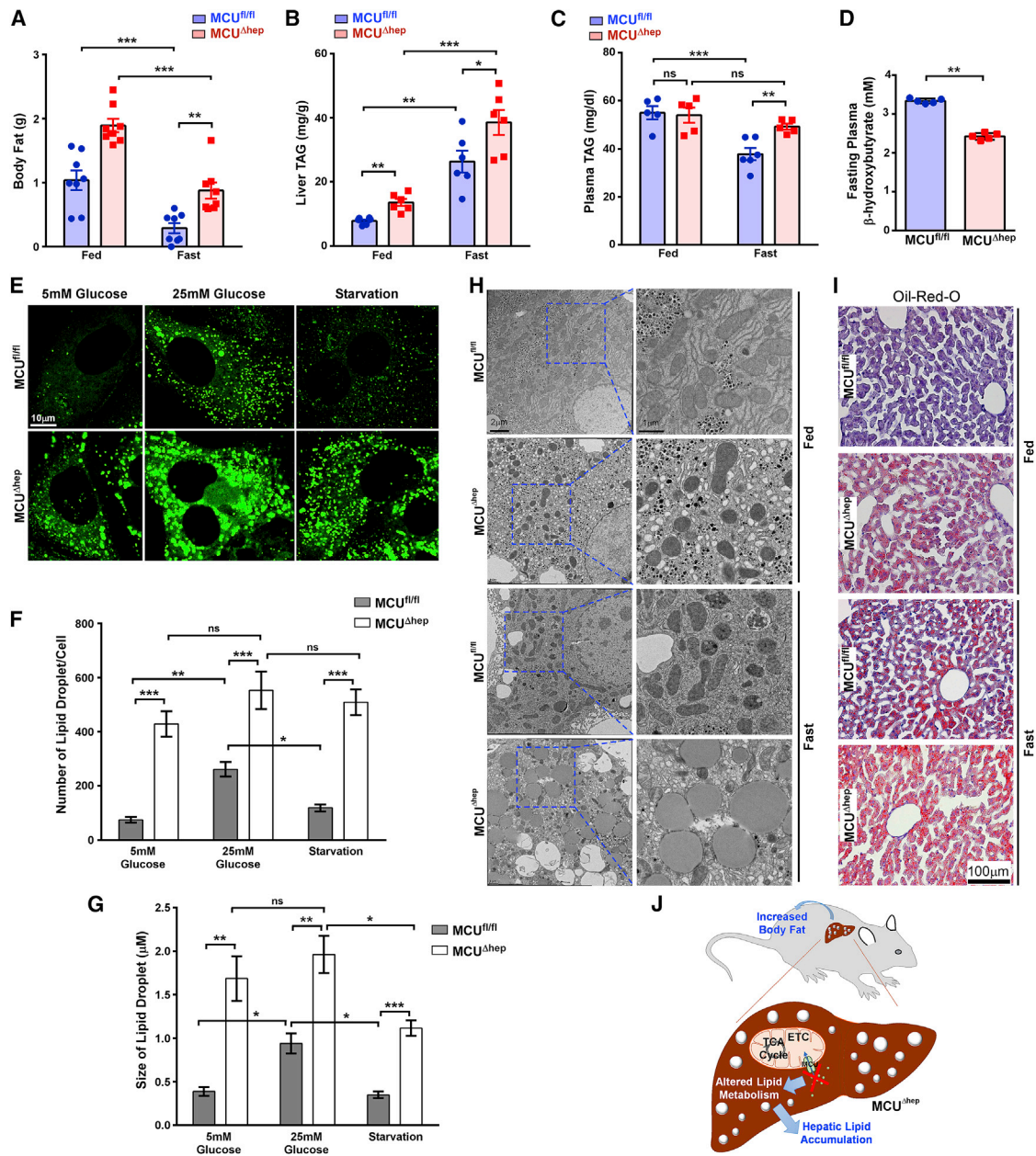
Figure 2. Loss of MCU Promotes Hepatic Lipid Accumulation and Increases Total Body Fat

(A) Body mass was monitored using NMR and DEXA before and after 24 h fasting. n = 11–12 mice per group.

(B) Liver triglycerides were measured using an enzymatic assay. n = 4–6 mice per group.

(C) Hepatic deletion of MCU results in increased plasma TAG in the fasting state, as measured by enzymatic assay. n = 5–6 mice per group.

(D) MCU$^{\Delta hep}$ mice showed decreased plasma ketones under the fasting state, as measured by enzymatic assay. n = 5 mice per group.

(E) Primary hepatocytes were isolated from MCU$^{fl/fl}$ and MCU$^{\Delta hep}$ mice and cultured in low glucose, high glucose, and high glucose followed by starvation. Lipid droplets were visualized by confocal microscopy. n = 3.

(F) Quantification of the number of lipid droplets from (E). n = 3.

(G) Quantification of the size of lipid droplets from (E). n = 15–30 cells from each isolation. n = 3.

(H) Representative electron micrograph showing a large number of lipid droplets in MCU KO hepatocytes. n = 3 mice per group.

(I) Representative histological section image showing massive oil red O staining in MCU KO liver. n ∼40 images. n = 3 mice.

(J) Schematic of hepatic ablation of MCU, showing increased lipid deposition in the liver, which subsequently increased the whole-body fat content.

Statistical analysis: mean ± SEM. *p < 0.05, **p < 0.01, ***p < 0.001.
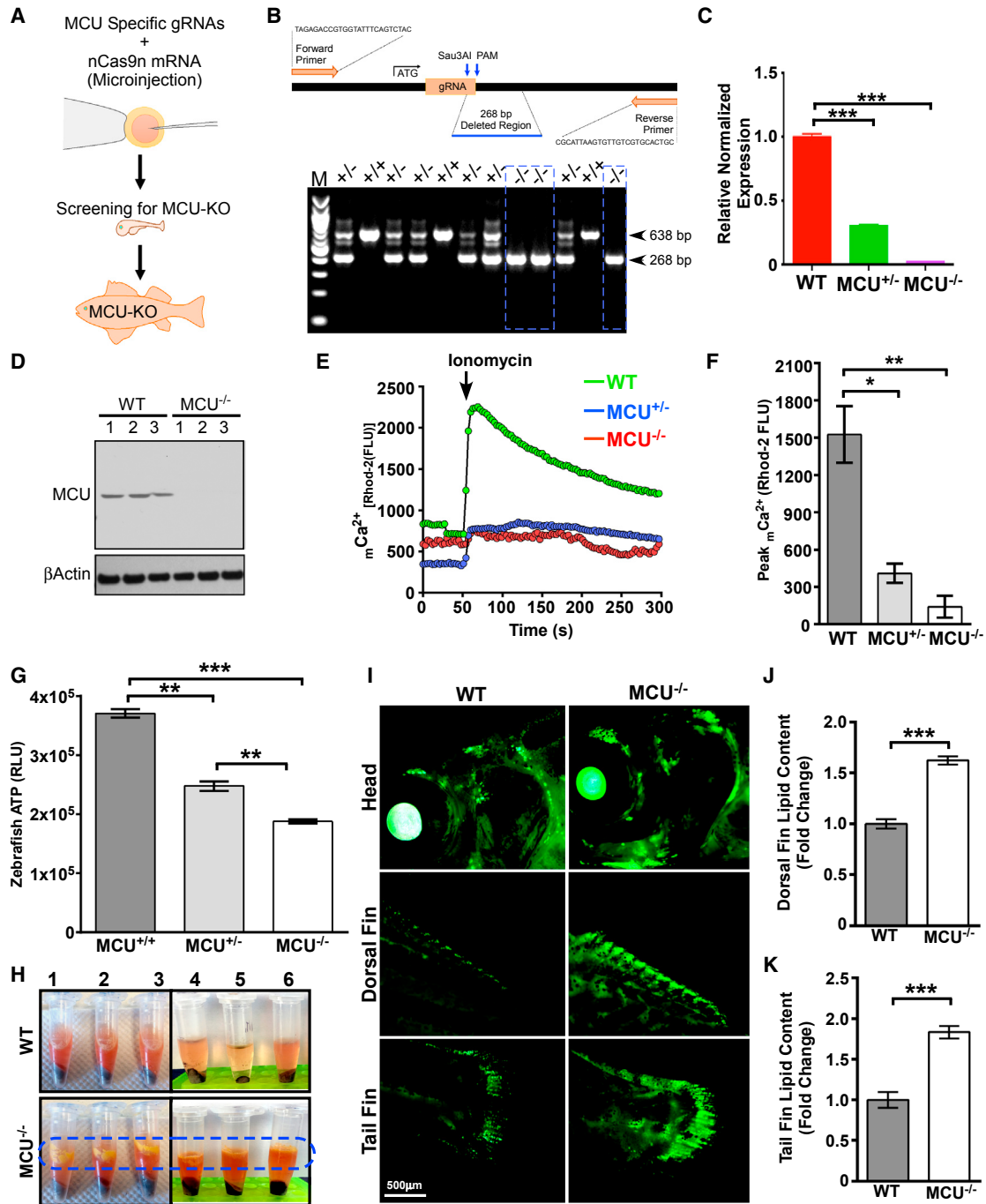
Figure 3. Loss of MCU Limits $_mCa^{2+}$ Uptake and Elevates Total Body Fat in Zebrafish

(A) Schematic of the generation of global MCU KO zebrafish using CRISPR/Cas9.

(B) Genotyping for MCU deletion.

(C) Bar graph showing MCU mRNA abundance in WT, MCU$^{+/-}$, and MCU$^{-/-}$ zebrafish.

(D) Western blot for MCU expression. n = 3.

(E) Measurement of $_mCa^{2+}$ uptake. n = 5–10.

(F) Quantification of ionomycin-induced peak $_mCa^{2+}$ levels from (E). n = 5–10.

(G) Bar graph representing cellular ATP levels in cells isolated from MCU$^{+/+}$, MCU$^{+/-}$, and MCU$^{-/-}$ zebrafish. n = 4.

(legend continued on next page)

hepatocytes were supplemented with exogenous palmitate in glucose-free medium. To confirm endogenous FAO involvement, etomoxir was used as an inhibitor of carnitine palmitoyl-transferase-1 (CPT-1). Basal and maximal FAO-coupled OCRs were significantly reduced in MCU$^{\Delta hep}$ hepatocytes compared with the control (Figures 1P and 1Q). CPT-1 expression was unchanged, indicating that the reduction in FAO-coupled OCR was not due to the alteration in mitochondrial fatty acid transport (Figures S1I and S1J). MCU$^{\Delta hep}$ hepatocytes did not display changes in the mitochondrial biogenesis-related transcription factors PGC1α, mitochondrial transcription factor A (mtTFA), and NRF1 (Figures S1K and S1L) but did show significant changes in the AMP:ATP ratio, consistent with the decreased OXPHOS activity (Figures 1R and 1S). These data clearly indicate that both glucose- and FAO-dependent OCRs and ATP production in hepatocytes are Ca^{2+}-dependent (Figure 1T).

Loss of *Mcu* Promotes Hepatic Lipid Accumulation and Lowers Ketone Body Production

We next investigated the broader metabolic effects of hepatocyte-specific *Mcu* ablation in mice. Although the body weight was approximately equivalent, the total body fat content of MCU$^{\Delta hep}$ mice was significantly increased during both the fed and fasting states (Figures 2A and S3A). The ratios of liver:body weight and white adipose tissue (WAT):body weight were also significantly increased in MCU$^{\Delta hep}$ mice (Figures S3B and S3C). Biochemical analysis of livers from MCU$^{\Delta hep}$ mouse livers revealed significant increases in fed and fasted triglycerides (TAGs) despite an increase in plasma TAGs being observed only in the fasting state (Figures 2B and 2C). During fasting, plasma ketones were significantly decreased in MCU$^{\Delta hep}$ mice (Figure 2D), suggesting a link between MCU-dependent $_mCa^{2+}$ and acetyl-coenzyme A (CoA) oxidation. Ten-week-old mice were subjected to three different states (fed, fasted, and re-fed) for assessment of food intake, locomotor activity, heat, fat utilization, O_2 consumption, and respiratory exchange ratio (RER). These whole-body metabolic parameters were unchanged between control and MCU$^{\Delta hep}$ mice (Figures S2A–S2F).

Hepatic lipid metabolism is tightly linked with glucose metabolism. Therefore, we assessed glucose homeostasis in MCU$^{\Delta hep}$ mice. Fasting and fed blood glucose levels, as well as glucose tolerance, were unchanged between MCU$^{fl/fl}$ and MCU$^{\Delta hep}$ mice (Figures S3D and S3E). Stored hepatic glycogen is the primary energy source during early fasting, and hepatocytes generate glucose from glycogen through glycogenolysis (Petersen et al., 2017). Interestingly, MCU$^{\Delta hep}$ mice showed increased glycogen during the fed state, with the same level of clearance in the fasting state (Figure S3F). MCU$^{fl/fl}$ and MCU$^{\Delta hep}$ hepatocytes had comparable glucose output, which suggests that deletion of hepatic *Mcu* does not compromise glycogenolysis (Figure S3G). MCU$^{\Delta hep}$ hepatocytes had normal glucose uptake (Figures S3H and S3I). This suggests that the elevated TAG

levels and reduced ketone bodies are possibly due to lower mitochondrial matrix Ca^{2+} in MCU$^{\Delta hep}$ mice.

We next investigated whether deletion of *Mcu* in hepatocytes led to lipid accumulation in the liver. Hepatocytes isolated from MCU$^{fl/fl}$ and MCU$^{\Delta hep}$ animals were cultured in the presence of low (5 mM) and high (25 mM) glucose, followed by starvation. MCU$^{\Delta hep}$ hepatocytes retained significantly higher levels of lipid vesicles compared with the control (Figures 2E–2G). Upon starvation, lipids were depleted in control but not in MCU$^{\Delta hep}$ hepatocytes, suggesting a lack of fat mobilization (Figures 2F and 2G). In addition to the number of lipid droplets, the size of the lipid droplets was significantly larger in MCU$^{\Delta hep}$ hepatocytes (Figure 2G). Consistent with confocal imaging analysis, ultrastructural studies revealed increased accumulation of lipid droplets in MCU$^{\Delta hep}$ mice under fed and fasting conditions (Figure 2H). Oil red O staining of liver sections recapitulated this and revealed extensive lipid staining in MCU$^{\Delta hep}$ liver sections (Figure 2I). Hepatic lipid accumulation has been linked to increased endoplasmic reticulum (ER) stress; however, MCU$^{\Delta hep}$ hepatocytes have an intact ER with no sign of stress (Figures S3J and S3K).

We asked whether *Mcu* deletion induces acute hepatic inflammation. Plasma alanine aminotransferase (ALT) levels were found to be unchanged between MCU$^{fl/fl}$ and MCU$^{\Delta hep}$ mice (Figure S3L). H&E staining of both MCU$^{fl/fl}$ and MCU$^{\Delta hep}$ mouse livers revealed no infiltration of inflammatory cells in MCU$^{\Delta hep}$ tissue (Figure S3M). We next investigated whether loss of *Mcu* has any effect on liver TAG secretion and *de novo* lipogenesis. Analysis of liver TAG secretion and hepatic and white adipose lipogenesis were found to be unchanged between MCU$^{fl/fl}$ and MCU$^{\Delta hep}$ mice (Figures S3N–S3P), indicating that hepatic lipid accumulation in MCU$^{\Delta hep}$ mice could be due to decreased fatty acid utilization as a result of MCU deletion (Figure 2J).

Genetic Ablation of *Mcu* Limits $_mCa^{2+}$ Uptake and Elevates Total Body Fat in Zebrafish

Because liver-specific deletion of *Mcu* in mice with the C57BL/6 genetic background caused aberrant lipid accumulation, the zebrafish model system could address the conservation of this mechanism across species. Adaptation of the CRISPR/Cas9 gene editing strategy eliminates morpholino-induced false positive and negative genetic mutant phenotypes (Figure 3A; Clark et al., 2011). We targeted a region proximal to the *Mcu* translation initiation codon and confirmed the 268-bp deletion allele by DNA sequencing, qRT-PCR, and western blotting (Figures 3B–3D). Isolated primary zebrafish cells were used to assess the $_mCa^{2+}$ dynamics for both control and MCU knockout (KO) zebrafish. As expected, $_mCa^{2+}$ uptake was significantly reduced in MCU KO zebrafish without altering $\Delta\Psi_m$ (Figures 3E, 3F, S4A, and S4B). Similar to MCU$^{\Delta hep}$ hepatocytes, cellular ATP levels were lower in MCU KO zebrafish and, to a lesser extent, in MCU$^{+/-}$ cells (Figure 3G). During zebrafish cell isolation, we found that supernatants collected from MCU KO zebrafish cells

---

(H) Adult WT and MCU$^{-/-}$ zebrafish were homogenized and centrifuged. MCU$^{-/-}$ zebrafish samples show a clear yellow color lipid layer on top of the protein lysate. n = 6.

(I) Adult WT and MCU$^{-/-}$ zebrafish were stained with Lipid Green to monitor the distribution of lipids in the whole body. n = 3.

(J and K) Bar graphs represent the quantification of Lipid Green staining from the dorsal (J) or tail (K) fin. n = 3.

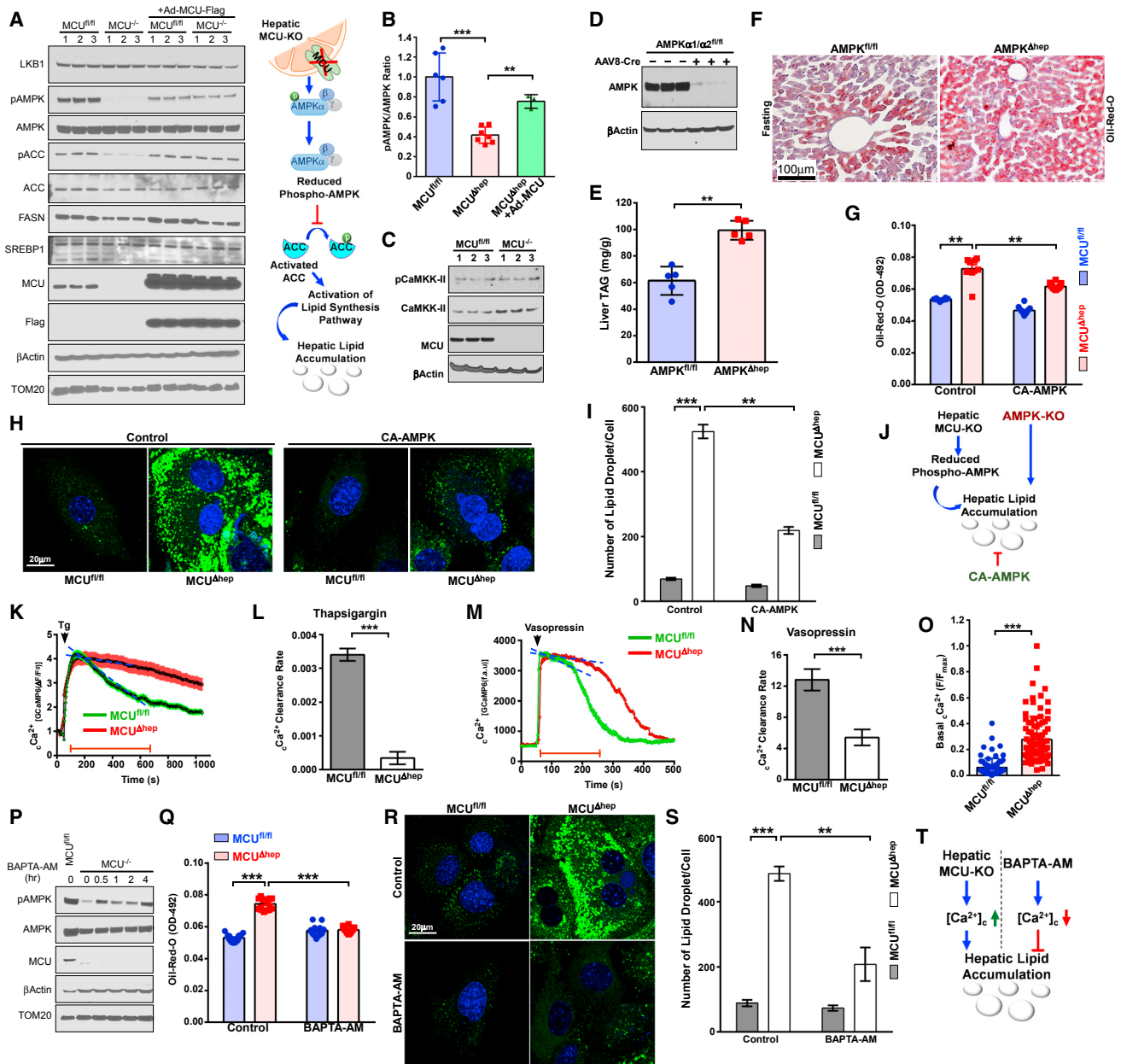Statistical analysis: mean ± SEM. *p < 0.05, **p < 0.01, ***p < 0.001.

Figure 4. Ablation of $_m$Ca^{2+} Uptake Augments the $_c$Ca^{2+} Rise That Enhances AMPK Dephosphorylation

(A) Hepatocytes isolated from MCU$^{fl/fl}$ and MCU$^{\Delta hep}$ mice were lysed in radioimmunoprecipitation assay (RIPA) buffer and immunoblotted for the indicated antibodies. n = 6.

(B) Bar graph representing the pAMPK:AMPK ratio from (A). n = 6.

(C) Immunoblot analysis for phospho and total CaMKK-II. n = 6.

(D) Hepatocyte lysates from AMPKα1/α2$^{fl/fl}$ and AMPKα1/α2$^{fl/fl}$Cre+ mice were probed for AMPKα protein abundance. n = 3.

(E) Hepatic TAG levels. n = 5.

(F) Assessment of hepatic lipid accumulation by Oil-Red-O staining. n = 5.

(G) Primary hepatocytes isolated from MCU$^{fl/fl}$ and MCU$^{\Delta hep}$ mice were infected with a CA-AMPK-expressing adenovirus. Hepatocytes were stained with oil red O and measured. n = 6–12 replicates from 3 mice.

(H) Visualization of lipid droplets from CA-AMPK reconstituted MCU$^{\Delta hep}$ hepatocytes. n = 3.

(I) Quantification of the number of lipid droplets from (H). n = 20–30 cells. n = 3.

(J) Schematic depicting a link between MCU and AMPK phosphorylation.

(K) GCaMP6-expressing hepatocytes from MCU$^{fl/fl}$ and MCU$^{\Delta hep}$ were stimulated with thapsigargin (Tg) or Vasopressin, and $_c$Ca^{2+} dynamics were monitored. n = 3.

(L) Quantification of the $_c$Ca^{2+} clearance rate from (K). n = 15–25 cells. n = 3.

(legend continued on next page)

appeared to have a strikingly higher fat content that was visually apparent (Figure 3H). We therefore extended the *in vitro* observation to the *in vivo* imaging approach of fat deposition in intact live zebrafish. The fluorescence intensity of lipids in the dorsal fin and tail fin were considerably increased (Figures 3I–3K), further supporting our results in MCU$^{\Delta hep}$ mice showing that MCU deletion results in higher lipid accumulation.

MCU Deletion in Hepatocytes Restrains Nutrient Sensing through Altered $_cCa^{2+}$ Signaling

MCU-mediated $_mCa^{2+}$ plays an essential role in mitochondrial bioenergetics and is required for maintenance of hepatic ATP content (Figure 1). Having observed elevated TAGs and decreased ketone body levels in MCU$^{\Delta hep}$ mice, we speculated that the decreased ATP levels might activate signaling via the energy-sensing AMPK (Hardie, 2015; Hardie et al., 2012; Kahn et al., 2005; Mihaylova and Shaw, 2011). In contrast to our expectations, MCU deletion resulted in a large reduction in T172-phosphorylated (active) AMPK-α, whereas total AMPK protein and mRNA levels remained unchanged (Figures 4A, 4B, and S5A). Expression of the upstream kinases LKB1 and calcium-regulated kinase calcium/calmodulin dependent protein kinase kinase-II (CaMKK-II) remained unchanged (Figures 4A and 4C). However, downstream inhibitory phosphorylation of acetyl-CoA carboxylase (ACC) was decreased (Figure 4A). Expression of two other key proteins involved in lipid synthesis, fatty acid synthase and SREBP1, remained unchanged (Figure 4A). Adenoviral reconstitution of MCU in MCU$^{\Delta hep}$ hepatocytes restored phosphorylation of AMPK (Figure 4A). To rule out a global dephosphorylation event, we also monitored extracellular signal-regulated kinase (ERK) phosphorylation and found normal ERK phosphorylation in MCU KO hepatocytes (Figure S5B). To confirm the potential of impaired AMPK signaling to drive hepatic lipid accumulation in MCU$^{\Delta hep}$ mice, we next generated hepatic AMPK-KO (AMPK$^{\Delta hep}$) mice by injecting adenovirus-associated virus 8-Cre (AAV8-Cre) into AMPKα1/α2$^{fl/fl}$ mice, which have LoxP sites flanking both the AMPKα1 and AMPKα2 loci. The loss of AMPK protein was validated by western blotting (Figure 4D). Biochemical analysis of hepatic tissue collected from overnight-fasted mice showed significant hepatic lipid accumulation in AMPK$^{\Delta hep}$ mice (Figure 4E). This observation was further validated by oil red O staining of liver tissue section and borondipyrromethene (BODIPY) staining of primary hepatocytes (Figures 4F, S5C, and S5D). However, the loss of AMPK did not affect $_mCa^{2+}$ uptake or $\Delta\Psi_m$ (Figures S5E and S5F), indicating that AMPK is downstream of MCU in lipid accumulation. The involvement of AMPK was further confirmed by using consti-

tutively active AMPK (AMPKα1 T172D, hereafter called CA-AMPK) (Hardie, 2011; King et al., 2009). Primary hepatocytes isolated from MCU$^{fl/fl}$ and MCU$^{\Delta hep}$ mice were infected with an CA-AMPK-expressing adenovirus and monitored for lipid accumulation (Figures 4G–4J and S5G).

Blockade of $_mCa^{2+}$ Uptake Augments a $_cCa^{2+}$ Rise that Enhances AMPK Dephosphorylation

To decipher the underlying mechanism of AMPK dephosphorylation in MCU$^{\Delta hep}$ mice, we investigated whether loss of MCU has any effect on $_cCa^{2+}$ dynamics. Hepatocytes were infected with an adenovirus expressing the $_cCa^{2+}$-reporter GCaMP6, and $_cCa^{2+}$ dynamics were monitored in response to thapsigargin and vasopressin. The MCU$^{\Delta hep}$ hepatocytes exhibited delayed $_cCa^{2+}$ clearance after stimulation with thapsigargin and vasopressin (Figures 4K–4N). Remarkably, basal $_cCa^{2+}$ was elevated in MCU$^{\Delta hep}$ hepatocytes (Figure 4O). Because loss of MCU caused persistent elevation of $_cCa^{2+}$, we investigated whether chelation of $_cCa^{2+}$ restores the phosphorylated form of AMPK in MCU$^{\Delta hep}$ hepatocytes. When hepatocytes were pretreated with 1,2-Bis (2-aminophenoxy)ethane-N,N,N′,N′-tetraacetic acid tetrakis (acetoxymethyl ester) (BAPTA-AM; 25 μM), a significant amount of phosphorylated AMPK was detected, even as early as 30 min (Figure 4P). Next, we investigated whether BAPTA-AM-mediated chelation of $_cCa^{2+}$ improves lipid clearance in MCU$^{\Delta hep}$ hepatocytes. Interestingly, chelation of $_cCa^{2+}$ reduced the lipid content in MCU$^{\Delta hep}$ hepatocytes, as indicated by oil red O and BODIPY staining (Figures 4Q–4S). Collectively, these data indicate that blockade of $_mCa^{2+}$ buffering results in AMPK dephosphorylation through aberrant $_cCa^{2+}$ elevation, leading to hepatic lipid accumulation in MCU$^{\Delta hep}$ mice (Figure 4T).

Cytosolic Ca^{2+} Rise Augments AMPK Dephosphorylation through Protein Phosphatase-4

Having determined that AMPK dephosphorylation is a $_cCa^{2+}$-dependent signal, we used pharmacologic and genetic tools to identify the phosphatase responsible for AMPK dephosphorylation. The pan protein phosphatase inhibitor (PP1, PP2A, PP2B, and PP4 inhibitor) okadaic acid restored AMPK phosphorylation, suggesting a phosphatase dependent-event (Figure 5A). Because AMPK dephosphorylation is a $_cCa^{2+}$-dependent protein phosphatase and calcineurin is a Ca^{2+}-calmodulin-activated protein phosphatase, we tested whether FK506 would prevent AMPK dephosphorylation. FK506 pretreatment did not restore AMPK phosphorylation in MCU$^{\Delta hep}$ mice (Figure 5B). We asked whether the Ca^{2+}-dependent, ubiquitously expressed PP2A subfamily phosphatase PP4 could be

---

(M) GCaMP6-expressing hepatocytes from MCU$^{fl/fl}$ and MCU$^{\Delta hep}$ were stimulated with Vasopressin and $_cCa^{2+}$ dynamics were monitored. n = 3.

(N) Quantification of the $_cCa^{2+}$ clearance rate from (M). n = 15–25 cells. n = 3.

(O) Hepatocytes isolated from MCU$^{fl/fl}$ and MCU$^{\Delta hep}$ adult mice were transduced with an adenovirus expressing the $_cCa^{2+}$ sensor GCaMP6, and basal $_cCa^{2+}$ fluorescence was quantified. n = 74–91 cells from 3 mice in each group.

(P) Hepatocytes were treated with the intracellular Ca^{2+} chelator BAPTA-AM for various times. Cell lysates were immunoblotted for the indicated antibodies. n = 4.

(Q) Hepatocytes were treated with BAPTA-AM overnight, and oil red O stain was quantified. 12 replicates from 3 mice per group.

(R) Visualization of lipid droplets from control and BAPTA-AM-treated hepatocytes. n = 3 mice per group.

(S) Quantification of lipid droplets from control and BAPTA-AM-treated hepatocytes. n = 20–30 cells per group. n = 3 mice per group.

(T) Schematic depicting how $_cCa^{2+}$ determines lipid clearance, possibly through AMPK phosphorylation.

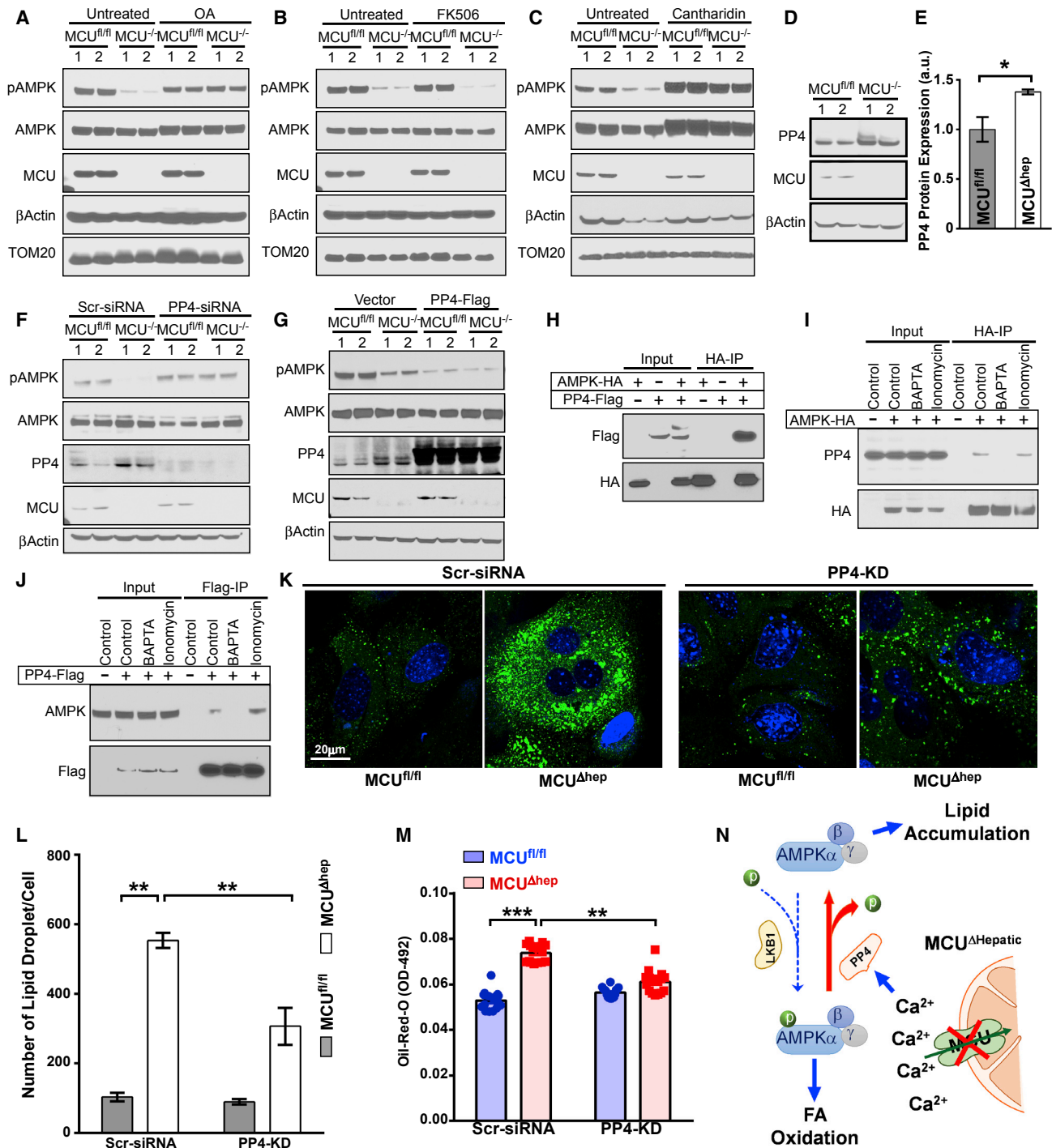Statistical analysis: mean ± SEM. **p < 0.01, ***p < 0.001.

Figure 5. AMPK Dephosphorylation in MCU KO Hepatocytes Is Likely Due to PP4

(A) Hepatocytes were treated with okadaic acid (OA) (50 nM) for 2 h. Cell lysates were immunoblotted for the indicated antibodies. n = 4.

(B) MCU$^{fl/fl}$ and MCU$^{\Delta hep}$ hepatocytes were treated with FK506 (2 μM) for 2 h and immunoblotted for the indicated antibodies. n = 4.

(C) MCU$^{fl/fl}$ and MCU$^{\Delta hep}$ hepatocytes were treated with cantharidin (50 μM) for 2 h and immunoblotted for the indicated antibodies. n = 4.

(D) Hepatocytes isolated from MCU$^{fl/fl}$ and MCU$^{\Delta hep}$ mice were lysed and immunoblotted for the indicated antibodies. n = 4.

(E) Densitometric analysis of PP4 protein abundance. n = 4.

(F) Hepatocytes were transfected with PP4 siRNA for 72 h. Cell lysates were immunoblotted for the indicated antibodies. n = 4.

(G) Hepatocytes were transfected with PP4-FLAG for 48 h. Cell lysates were immunoblotted for the indicated antibodies. n = 4.

(legend continued on next page)

responsible for AMPK dephosphorylation (Shui et al., 2007). Pre-treating MCU$^{\Delta hep}$ hepatocytes with the PP4 inhibitor cantharidin restored the phosphorylated form of AMPK (Figure 5C). We also found that PP4 protein expression was increased in MCU$^{\Delta hep}$ hepatocytes (Figures 5D and 5E), indicating a $_cCa^{2+}$-regulated increased PP4 protein abundance. To verify the involvement of PP4 in AMPK dephosphorylation, we silenced PP4 expression in MCU$^{\Delta hep}$ hepatocytes using small interfering RNA (siRNA) (Figure 5F). PP4 knockdown resulted in restoration of AMPK phosphorylation (Figure 5F). Next we used the reverse approach to confirm the involvement of PP4 in AMPK dephosphorylation by ectopic expression of PP4. Overexpression of PP4-FLAG resulted in dephosphorylation of AMPK in MCU$^{fl/fl}$ hepatocytes that was further enhanced in MCU$^{\Delta hep}$ hepatocytes, demonstrating PP4 to be a major phosphatase of AMPK in the liver (Figure 5G). To identify whether AMPK and PP4 exist as a Ca^{2+}-dependent protein complex, we performed protein-protein interaction studies, which demonstrated that AMPK and PP4 bind one another (Figure 5H) and that this binding is regulated by $_cCa^{2+}$ (Figures 5I and 5J). Silencing of PP4 in MCU$^{\Delta hep}$ hepatocytes decreased the lipid content, as indicated by oil red O and BODIPY staining (Figures 5K–5M). These findings reveal that the blockade of rapid sequestration of Ca^{2+} into the mitochondrial matrix by MCU deletion results in activation of Ca^{2+}-dependent PP4, which dephosphorylates AMPK (Figure 5N).

The Gain-of-Function MCU Controls PP4, which Enhances Hepatic Lipid Clearance during Fasting

We sought to understand whether MCU hyperactivation has the potential for higher lipid mobilization and increased FAO. A recent report revealed that the human MCU C97A mutation results in hyperactivation of MCU channel activity (Figure S6A; Dong et al., 2017). Therefore, we generated a gain-of-function MCU mouse model (C96A-knockin [KI]) with a global MCU C96A (corresponding to human MCU C97) KI using the CRISPR/Cas9 approach (Figures 6A and S6B), which was confirmed by restriction fragment length polymorphism (RFLP) and Sanger sequencing (Figures 6A and S6C). The C96A-KI mice were viable (Figure 6B) but had reduced body weight compared with the WT control (Figures 6C and S6D). We investigated the $_mCa^{2+}$ dynamics and noted that C96A-KI hepatocytes exhibited an increased $_mCa^{2+}$ uptake rate as well as higher basal matrix $_mCa^{2+}$ under normal $\Delta\Psi_m$ (Figures 6D–6G, S6E, and S6F). Although western blot analysis of OXPHOS proteins revealed no differences between WT and C96A-KI hepatocytes (Figure 6H), C96A-KI hepatocytes exhibited higher basal and maximal OCRs (Figures 6I and 6J).

Next we monitored the AMPK and ACC phosphorylation status and the expression of PP4 in C96A-KI hepatocytes. C96A-KI he-

patocytes had higher levels of phosphorylated AMPK and ACC and a significant reduction in PP4 protein abundance (Figures 6K–6M). Biochemical analysis of hepatic tissue from C96A-KI mice clearly showed a reduction in liver and plasma TAG levels along with a significant increase in plasma ketone levels (Figures 6N–6P). We next investigated the effect of C96A-KI on high-glucose-induced lipid accumulation in primary hepatocytes. C96A-KI hepatocytes showed a clear reduction in lipid droplet accumulation under high-glucose conditions (Figures 6Q and 6R). In support of these data, oil red O staining confirmed enhanced lipid clearance by C96A-KI mice during fasting (Figure 6S). This newly generated mouse model further validates the involvement of MCU in the regulation of hepatic lipid homeostasis.

Restoration of AMPK Phosphorylation in MCU$^{\Delta hep}$ Mice Improves Lipid Clearance

It has been shown that cells treated with metformin exhibit increased AMPK phosphorylation (Hawley et al., 2002; Madiraju et al., 2014; Shaw et al., 2005; Zhou et al., 2001). Metformin treatment did not alter $_mCa^{2+}$ uptake (Figure S7A). We next tested whether supplementing metformin would promote AMPK phosphorylation and lipid clearance in MCU$^{\Delta hep}$. MCU$^{\Delta hep}$ hepatocytes treated with metformin had significantly increased AMPK phosphorylation, similar to the effect of 5-aminoimidazole-4-carboxamide ribonucleotide (AICAR) (Figures 7A and 7B). Given the effect of metformin on AMPK phosphorylation and fatty acid metabolism, we examined whether metformin administration could deplete lipid accumulation in MCU$^{\Delta hep}$ mice. After 3 weeks of oral metformin administration (1.25 mg/mL), we noted a marked reduction in lipid content in MCU$^{\Delta hep}$ livers, as evidenced by oil red O staining (Figure 7C). Similarly, acute metformin treatment markedly reduced hepatocyte lipid content, as evidenced by BODIPY-positive lipid vesicle numbers (Figures 7D and 7E), but did not normalize the remaining lipid droplet size (Figure S7B).

Finally, we conducted a comprehensive lipidomics analysis and characterized the lipid species in control, MCU$^{\Delta hep}$, and metformin-treated MCU$^{\Delta hep}$ mice. Lipidomics analysis of MCU$^{\Delta hep}$ liver tissue showed a significant accumulation of TAG and diacyl-glycerol (DAG) lipid species (Figures 7F, 7G, S7C, and S7D). Notably, administration of metformin not only restored AMPK phosphorylation but also significantly lowered several TAG and DAG species (Figures 7F and 7G). Collectively, these data indicate that loss of MCU results in altered hepatic lipid metabolism, leading to hepatic lipid accumulation and lipidomic remodeling.

DISCUSSION

We report that hepatic deletion of MCU lowers hepatic $_mCa^{2+}$, reduces FAO-coupled mitochondrial respiration, and increases

---

(H–J) HepG2 cells were transfected with AMPK-hemagglutinin (HA) and PP4-FLAG plasmids for 48 h. Cell lysates were immunoprecipitated with an HA antibody and probed with the indicated antibodies (H). Under a similar condition (I and J), cells were treated with BAPTA-AM in the presence or absence of ionomycin (50 nM) stimulation. The reciprocal immunoprecipitation was performed with HA or FLAG antibodies and probed with the indicated antibodies. n = 3.

(K) Visualization of lipid droplets from scrambled (Scr) siRNA- and PP4 siRNA-treated hepatocytes. n = 3.

(L) Quantification of lipid droplets from Scr siRNA- and PP4 siRNA-treated hepatocytes. n = 20–30 cells. n = 3.

(M) Hepatocytes isolated from MCU$^{fl/fl}$ and MCU$^{\Delta hep}$ adult mice were transfected with PP4 siRNA for 72 h. Cells were stained with oil red O and quantified. n = 3.

(N) Schematic depicting aberrant $_cCa^{2+}$ clearance in MCU KO hepatocytes exhibiting AMPK dephosphorylation through elevated PP4 activity.

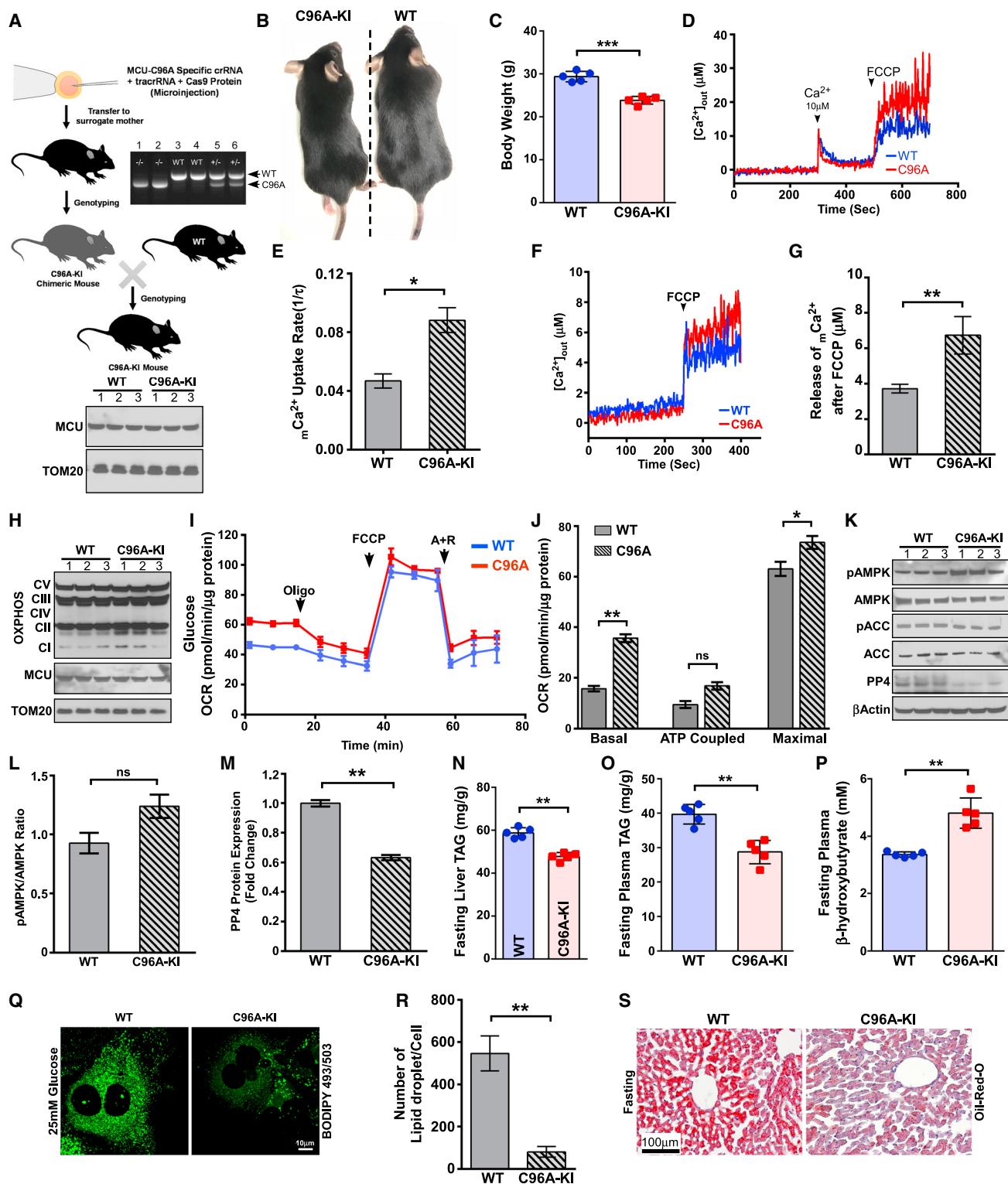Statistical analysis: mean ± SEM. *p < 0.05, **p < 0.01, ***p < 0.001.

Figure 6. Hepatocytes Harboring MCU-C96A Display Reduced PP4 and Augmented Hepatic Lipid Clearance during Fasting

(A) Schematic depicting the strategy used to generate MCU-C96A KI mice. Top right: genotyping of MCU-C96A KI mice. Bottom: MCU protein abundance.

(B) 12-week-old MCU-C96A KI mice are viable.

(C) MCUC96A-KI mice have reduced body weight at 12 weeks. n = 5.

(D) MCU-mediated extramitochondrial Ca^{2+} clearance and $_mCa^{2+}$ uptake. n = 3.

(legend continued on next page)

hepatic lipid accumulation, linking $_mCa^{2+}$ handling to hepatic lipid metabolism. Our characterization of this mouse model reveals that, following MCU ablation, there is an accumulation of $_cCa^{2+}$ because of a lack of $_mCa^{2+}$ sequestration via MCU into the matrix. This observation is in contrast to earlier reports heart- and endo-thelium-specific MCU KO models, in which no apparent changes were observed in $_mCa^{2+}$ (Luongo et al., 2015; Pan et al., 2013; Tomar et al., 2016). Depletion of $_mCa^{2+}$ and reduced $_cCa^{2+}$ clearance ability in MCU$^{\Delta hep}$ hepatocytes indicates that MCU could be a major player in shaping metabolic outcomes in the liver. Although $_mCa^{2+}$ overload is necessary for PTP opening and mito-chondrial dysfunction, MCU KO failed to protect against cell death under ionomycin and oxidative stress conditions, signi-fying the physiological importance of $_mCa^{2+}$ buffering and cell survival (Nemani et al., 2018; Pan et al., 2013). Recently, it has been demonstrated that prevention of MCU-mediated Ca^{2+} up-take exhibited enhanced mitochondrial shape transition through Miro-1 and triggered cell death in a PTP-independent pathway (Nemani et al., 2018) Alternatively, MCU-dependent Ca^{2+} en-hances mitochondrial constriction, which is Drp1-independent, suggesting that Ca^{2+} dynamics may be an initiator of precon-struction (Chakrabarti et al., 2018). Nevertheless, altering $_mCa^{2+}$ may contribute significantly to changes in the mitochondrial phenotype and cellular metabolism.

It has been established that the $_cCa^{2+}$ clearance mechanisms operate differentially between tissues (Fieni et al., 2012; Paillard et al., 2017; Pan et al., 2013). For example, there are several rea-sons why one could speculate that $_mCa^{2+}$ remained unchanged in myocytes after MCU deletion. The extracellularly and intracel-lularly mediated $_cCa^{2+}$ rise is rapidly cleared by the high-Ca^{2+}-affinity sarcoplasmic or endoplasmic reticulum Ca^{2+} ATPase (SERCA) and plasma membrane pumps (plasma membrane Ca^{2+} ATPase [PMCA]) and sodium Ca^{2+} exchanger (NCX) in cardiomyocytes (Fearnley et al., 2011), where $\Delta\Psi_m$ and mito-chondrial buffering capacity is weaker because of excitation-contraction (E-C) coupling. In non-excitable cell types like hepatocytes, MCU clears $_cCa^{2+}$ faster than SERCA and PMCA pumps. Because $_mCa^{2+}$ uptake is primarily driven by the electro-chemical gradient across the mitochondrial inner membrane, it is possible that hepatocyte mitochondria are maintained in a hy-perpolarized state specifically to facilitate $_cCa^{2+}$ clearance and

maintain heterogeneity (Collins et al., 2002; Kuznetsov et al., 2004). Another striking difference we observed in hepatocytes was the reduction of both glucose and fatty acid-dependent mitochondrial OXPHOS. This further strengthens our finding of lower basal $_mCa^{2+}$ in MCU KO hepatocytes.

The most striking phenotype of MCU$^{\Delta hep}$ mice is dyslipidemia and ectopic accumulation of lipid in the liver, which was associ-ated with reduced fasting plasma ketones. These data suggest an impairment in FAO and, consequently, ketone body produc-tion in MCU KO hepatocytes. The lipid accumulation phenotype was observed in the mouse as well as zebrafish model systems, indicating conservation of MCU-regulated lipid metabolism across species. During starvation, AMPK promotes phosphory-lation and inactivation of ACC, which results in fatty acid uptake into mitochondria for β-oxidation (Hardie et al., 2012). Remark-ably, loss of MCU in the liver caused impairment of FAO and massive accumulation of total lipids under fasting conditions, suggesting the possibility that AMPK activity is impaired by the dysregulated cellular Ca^{2+} dynamics (Figures 4K–4O). As pre-dicted, deletion of MCU in hepatocytes caused delayed $_cCa^{2+}$ clearance under basal and hormonal stimulation. Activation of AMPK by increased AMP:ATP is well-established in the literature, but our findings demonstrate that, despite greatly decreased ATP and increased AMP in MCU KO hepatocytes, there was decreased AMPK activation (Figures 1S and 4A). In follow-up studies, we tested whether loss of AMPK alone was sufficient to confer a fatty liver phenotype. Interestingly, liver-specific AMPK KO mice displayed similar hepatic lipid accumu-lation, confirming the central role of AMPK in MCU KO-induced hepatic lipid accumulation. Chelation of $_cCa^{2+}$ restored phos-pho-AMPK levels in MCU KO hepatocytes, confirming the effect of Ca^{2+}-dependent regulation (Figure 4P).

It has been demonstrated that, in addition to its regulation by AMP, AMPK is activated by the upstream kinases LKB1 and CaMKK-II, which phosphorylate a conserved Thr172 in the α sub-unit (Hawley et al., 2005; Hurley et al., 2005; Woods et al., 2003). CaMKK-II activates AMPK via phosphorylation of the α subunit in the presence of increased $_cCa^{2+}$ (Hawley et al., 2005; Hurley et al., 2005). Because we propose a model of Ca^{2+}-mediated regulation of AMPK, it is pertinent to question whether CaMKK-II plays a role in this mechanism because of its known Ca^{2+}-induced activation.

(E) MCU-mediated $_mCa^{2+}$ uptake rate was calculated from (D). n = 3.

(F) Measurement of basal $_mCa^{2+}$ after addition of FCCP. n = 3.

(G) Quantification of basal $_mCa^{2+}$ after addition of FCCP from (F). n = 3.

(H) Western blot analysis of mitochondrial respiratory chain subunits of complex I (NDUFB8), complex II (succinate dehydrogenase complex iron sulfur subunit B [SDHB]), complex III (UQCRC2), complex IV (MTCO1), and ATP synthase subunit ATP5A. MCU and TOM20 were used as loading controls. n = 3.

(I) Measurement of mitochondrial OCR. n = 3.

(J) Measurement of basal, ATP coupled, and maximal OCR from (I). n = 3.

(K) Hepatocytes isolated from WT and C96A-KI mice were lysed and probed with the indicated antibodies. n = 3.

(L) Densitometric analysis of pAMPK/AMPK ratio from (K). n = 3.

(M) Densitometric analysis of PP4 protein expression from (K). n = 3.

(N) Measurement of liver and triglycerides (TAGs) under fasting conditions. Measurement of these parameters is described in Figure 2. n = 5.

(O) Measurement of plasma triglycerides (TAG) under fasting conditions. n = 5.

(P) Measurement of plasma ketone bodies under fasting conditions. n = 5.

(Q) Visualization of lipid droplets from WT and C96A KI hepatocytes. n = 3.

(R) Quantification of lipid droplets from (Q). n = 20–30 cells. n = 3.

(S) Representative histological section image shows reduced lipid accumulation in C96A-KI mice. n = 3 mice per group.

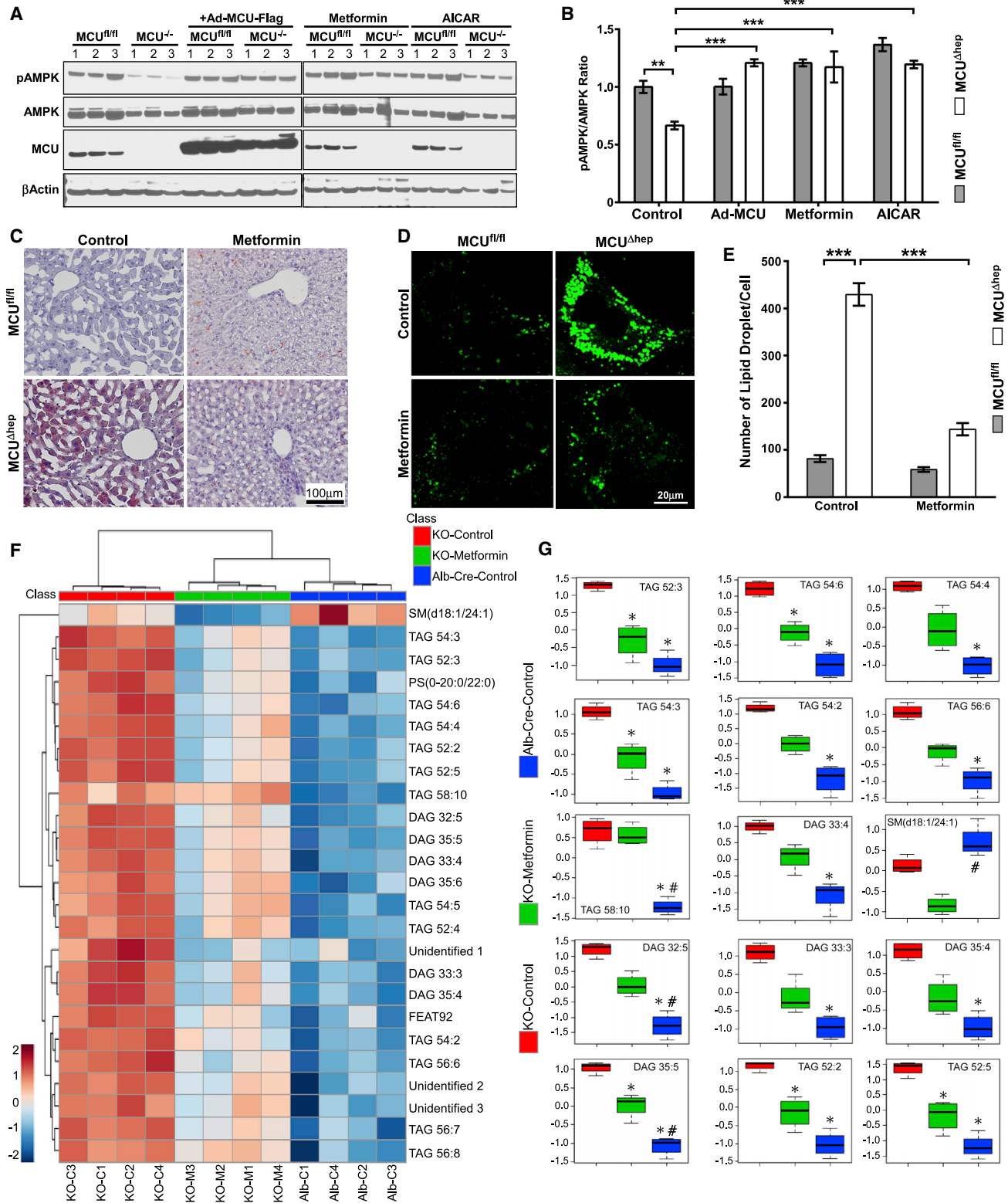Statistical analysis: mean ± SEM. *p < 0.05, **p < 0.01, ***p < 0.001.

Figure 7. Activation of AMPK by Metformin Corrects Hepatic Lipidome Remodeling in MCU KO Mice

(A) Hepatocytes isolated from MCU^fl/fl and MCU^Δhep treated with metformin (1 mM), AICAR (100 μM) for 16 hours. After treatment, cell lysates were probed with indicated antibodies. n = 3.

(legend continued on next page)

However, we did not observe any significant alteration in CaMKK-II phosphorylation in MCU$^{\Delta hep}$ mice. This finding is also consistent with studies that have demonstrated that CaMKK-II has limited distribution in hepatic tissue in comparison with neurons and T cells (Anderson et al., 1998; Mihaylova and Shaw, 2011). Surprisingly, our biochemical analysis found significant levels of AMPK dephosphorylation without any effect on the upstream kinases LKB1 and CaMKK-II in MCU KO hepatocytes, suggesting a mechanism of AMPK regulation independent of the canonical signaling cascade.

Although ATP antagonizes AMPK activation, dephosphorylation-dependent inactivation of AMPK is mediated by serine-threonine phosphatase proteins, including PP2A and PP2Cα (Hardie, 2011). Our search for a Ca^{2+}-dependent AMPK dephosphorylation mechanism revealed that pharmacologic inhibition of $_c$Ca^{2+}-regulated PP4 by cantharidin and knockdown of PP4 restored AMPK phosphorylation and reduced hepatic lipid accumulation in MCU KO hepatocytes (Figure 5). Our study demonstrates direct regulation of AMPK through Ca^{2+}-induced PP4 activity. To further test the physiological role of MCU, we created a unique gain-of-function MCU mouse model that displays higher $_m$Ca^{2+} uptake and rapidly clears $_c$Ca^{2+} (Figure 6). Interestingly, MCU C96A-KI mice not only exhibited higher MCU-mediated Ca^{2+} uptake but also reduced PP4 levels and lower circulating and hepatic TAGs in the fasted state.

The CA form of double ACC KI mice exhibits elevated lipogenesis and lower FAO, implying that AMPK activation is crucial for lipid clearance (Fullerton et al., 2013). Our data provide evidence that sustained $_c$Ca^{2+} elevation in MCU$^{\Delta hep}$ mice results in activation of ACC because of AMPK dephosphorylation and, consequently, lipid accumulation. Strikingly, our MCU C96A-KI mice restored AMPK and ACC phosphorylation states and rapid clearance of hepatic lipid during fasting. The insulin-sensitizing role of metformin has been linked to AMPK phosphorylation in the setting of obesity and insulin resistance (Howell et al., 2017; Li et al., 2011). Administration of metformin in MCU$^{\Delta hep}$ mice improved lipid clearance through MCU-independent AMPK phosphorylation, supporting a therapeutic intervention for disorders of hepatic insulin resistance and lipid accumulation.

STAR★METHODS

Detailed methods are provided in the online version of this paper and include the following:

- KEY RESOURCES TABLE
- CONTACT FOR REAGENT AND RESOURCE SHARING
- EXPERIMENTAL MODEL AND SUBJECT DETAILS
  - Mouse models
  - Zebrafish
  - Cell culture
- METHOD DETAILS
  - Isolation of mouse primary hepatocytes
  - Mitoplast I$_{MCU}$ patch-clamp recording
  - Measurement of mitochondrial Ca^{2+} uptake, $\Delta\Psi_m$, and mitochondrial matrix Ca^{2+}
  - Mitochondrial and cytosolic Ca^{2+} measurements using confocal live cell imaging system
  - Mitochondrial respiration measurements
  - Cellular AMP/ATP measurement
  - Mitochondrial reactive oxygen species measurement
  - TMRM staining for $\Delta\Psi_m$
  - Metabolic assessment of mice
  - Animal body composition, liver/plasma biochemistry, glucose tolerance test and glucose output assay
  - Lipid staining in primary hepatocytes, liver sections and whole zebrafish
  - Electron microscopy to visualize hepatic ultrastructure
  - Immunoblotting and co-immunoprecipitation assay
  - Global lipidomic profiling
- QUANTIFICATION AND STATISTICAL ANALYSIS

SUPPLEMENTAL INFORMATION

ACKNOWLEDGMENTS

AUTHOR CONTRIBUTIONS

D.T., P.J., F.J., C.C.D., and S. Srikantan performed hepatocyte isolation and culture, $_m$Ca^{2+} and $_c$Ca^{2+} measurements, confocal imaging, biochemical

---

(B) Bar graph showing the quantification of pAMPK in Figure 7A. n = 3.

(C) Representative histological section image shows clearance of lipids in MCU KO metformin-administered mice. n = 3.

(D) Visualization of lipid droplets from MCU$^{fl/fl}$ and MCU$^{\Delta hep}$ mice with or without metformin treatment. n = 3.

(E) Quantification of lipid droplets from (D). n = 15–30 cells per mice. n = 3.

(F) Lipids were analyzed as described in STAR Methods, and the identified features were subjected to a hierarchical cluster analysis. n = 4.

(G) Significant top 15 lipids (false discovery rate [FDR] = 0.001) representing the relative lipid modulation among the groups. The y axis represents normalized values. *, significantly different from MCU$^{\Delta hep}$; #, significantly different from metformin-administered MCU$^{\Delta hep}$. n = 4 per group.

Statistical analysis: mean ± SEM. *p < 0.05, **p < 0.01, ***p < 0.001.

assays, and mitochondrial respiration experiments. Z.D. isolated mitoplasts, and X.Z. performed patch-clamping. S.L.B., A.T., N.N., S. Shanmughapriya, A.M.W., M. Murray, and D.S. contributed reagents and experimental tools and performed mouse genotyping. D.T., R.R., A.S., S. Rhode, and S.H.R. performed liver histology and imaging. D.T., S. Rajan, and M. Madesh designed and established the mouse model. S. Rajan, A.V.M., D.B., and M. Madesh designed and developed the zebrafish model. D.T. and N.N. performed zebrafish confocal imaging. J.C. performed electron microscopy. D.S.W. performed liver lipidomics profiling. W.J.Q. and J.A.B. generated AMPKα1/α2$^{\Delta hep}$ mice. W.J.Q., J.A.B., L.N., K.S., and R.S.A. performed liver and plasma biochemistry and the *in vivo* CLAM study. S. Rajan, D.T., and S.L.B. performed molecular experiments, and guidance was provided by G.S.G., P.M., J.A.B., R.S.A., and M. Madesh. D.T. and M. Madesh conceived and designed the experiments and interpreted the experimental data. D.T., S.L.B., and M. Madesh wrote the manuscript with contributions from all the authors.

DECLARATION OF INTERESTS

The authors declare no competing interests.

REFERENCES

Alenghat, T., Meyers, K., Mullican, S.E., Leitner, K., Adeniji-Adele, A., Avila, J., Bućan, M., Ahima, R.S., Kaestner, K.H., and Lazar, M.A. (2008). Nuclear receptor corepressor and histone deacetylase 3 govern circadian metabolic physiology. Nature *456*, 997–1000.

Anderson, K.A., Means, R.L., Huang, Q.-H., Kemp, B.E., Goldstein, E.G., Selbert, M.A., Edelman, A.M., Fremeau, R.T., and Means, A.R. (1998). Components of a calmodulin-dependent protein kinase cascade. Molecular cloning, functional characterization and cellular localization of Ca2+/calmodulin-dependent protein kinase kinase β. J. Biol. Chem. *273*, 31880–31889.

Balaban, R.S. (2009). The role of Ca(2+) signaling in the coordination of mitochondrial ATP production with cardiac work. Biochim. Biophys. Acta *1787*, 1334–1341.

Baughman, J.M., Perocchi, F., Girgis, H.S., Plovanich, M., Belcher-Timme, C.A., Sancak, Y., Bao, X.R., Strittmatter, L., Goldberger, O., Bogorad, R.L., et al. (2011). Integrative genomics identifies MCU as an essential component of the mitochondrial calcium uniporter. Nature *476*, 341–345.

Bernardi, P. (1999). Mitochondrial transport of cations: channels, exchangers, and permeability transition. Physiol. Rev. *79*, 1127–1155.

Biasutto, L., Azzolini, M., Szabò, I., and Zoratti, M. (2016). The mitochondrial permeability transition pore in AD 2016: An update. Biochim. Biophys. Acta *1863*, 2515–2530.

Cárdenas, C., Miller, R.A., Smith, I., Bui, T., Molgó, J., Müller, M., Vais, H., Cheung, K.H., Yang, J., Parker, I., et al. (2010). Essential regulation of cell bioenergetics by constitutive InsP3 receptor Ca2+ transfer to mitochondria. Cell *142*, 270–283.

Chakrabarti, R., Ji, W.K., Stan, R.V., de Juan Sanz, J., Ryan, T.A., and Higgs, H.N. (2018). INF2-mediated actin polymerization at the ER stimulates mitochondrial calcium uptake, inner membrane constriction, and division. J. Cell Biol. *217*, 251–268.

Chaudhuri, D., Sancak, Y., Mootha, V.K., and Clapham, D.E. (2013). MCU encodes the pore conducting mitochondrial calcium currents. eLife *2*, e00704.

Clark, K.J., Balciunas, D., Pogoda, H.M., Ding, Y., Westcot, S.E., Bedell, V.M., Greenwood, T.M., Urban, M.D., Skuster, K.J., Petzold, A.M., et al. (2011). In vivo protein trapping produces a functional expression codex of the vertebrate proteome. Nat. Methods *8*, 506–515.

Collins, T.J., Berridge, M.J., Lipp, P., and Bootman, M.D. (2002). Mitochondria are morphologically and functionally heterogeneous within cells. EMBO J. *21*, 1616–1627.

De Stefani, D., Raffaello, A., Teardo, E., Szabò, I., and Rizzuto, R. (2011). A forty-kilodalton protein of the inner membrane is the mitochondrial calcium uniporter. Nature *476*, 336–340.

De Stefani, D., Rizzuto, R., and Pozzan, T. (2016). Enjoy the Trip: Calcium in Mitochondria Back and Forth. Annu. Rev. Biochem. *85*, 161–192.

Denton, R.M., and McCormack, J.G. (1980). The role of calcium in the regulation of mitochondrial metabolism. Biochem. Soc. Trans. *8*, 266–268.

Dong, Z., Shanmughapriya, S., Tomar, D., Siddiqui, N., Lynch, S., Nemani, N., Breves, S.L., Zhang, X., Tripathi, A., Palaniappan, P., et al. (2017). Mitochondrial Ca2+ Uniporter Is a Mitochondrial Luminal Redox Sensor that Augments MCU Channel Activity. Mol. Cell *65*, 1014–1028.e7.

Drago, I., Pizzo, P., and Pozzan, T. (2011). After half a century mitochondrial calcium in- and efflux machineries reveal themselves. EMBO J. *30*, 4119–4125.

Fearnley, C.J., Roderick, H.L., and Bootman, M.D. (2011). Calcium signaling in cardiac myocytes. Cold Spring Harb. Perspect. Biol. *3*, a004242.

Fieni, F., Lee, S.B., Jan, Y.N., and Kirichok, Y. (2012). Activity of the mitochondrial calcium uniporter varies greatly between tissues. Nat. Commun. *3*, 1317.

Foretz, M., Hébrard, S., Leclerc, J., Zarrinpashneh, E., Soty, M., Mithieux, G., Sakamoto, K., Andreelli, F., and Viollet, B. (2010). Metformin inhibits hepatic gluconeogenesis in mice independently of the LKB1/AMPK pathway via a decrease in hepatic energy state. J. Clin. Invest. *120*, 2355–2369.

Fu, S., Yang, L., Li, P., Hofmann, O., Dicker, L., Hide, W., Lin, X., Watkins, S.M., Ivanov, A.R., and Hotamisligil, G.S. (2011). Aberrant lipid metabolism disrupts calcium homeostasis causing liver endoplasmic reticulum stress in obesity. Nature *473*, 528–531.

Fullerton, M.D., Galic, S., Marcinko, K., Sikkema, S., Pulinilkunnil, T., Chen, Z.P., O'Neill, H.M., Ford, R.J., Palanivel, R., O'Brien, M., et al. (2013). Single phosphorylation sites in Acc1 and Acc2 regulate lipid homeostasis and the insulin-sensitizing effects of metformin. Nat. Med. *19*, 1649–1654.

Gilabert, J.A., and Parekh, A.B. (2000). Respiring mitochondria determine the pattern of activation and inactivation of the store-operated Ca(2+) current I(CRAC). EMBO J. *19*, 6401–6407.

Glancy, B., and Balaban, R.S. (2012). Role of mitochondrial Ca2+ in the regulation of cellular energetics. Biochemistry *51*, 2959–2973.

Glancy, B., Willis, W.T., Chess, D.J., and Balaban, R.S. (2013). Effect of calcium on the oxidative phosphorylation cascade in skeletal muscle mitochondria. Biochemistry *52*, 2793–2809.

Hajnóczky, G., Hager, R., and Thomas, A.P. (1999). Mitochondria suppress local feedback activation of inositol 1,4, 5-trisphosphate receptors by Ca2+. J. Biol. Chem. *274*, 14157–14162.

Hajnóczky, G., Csordás, G., Madesh, M., and Pacher, P. (2000). The machinery of local Ca2+ signalling between sarco-endoplasmic reticulum and mitochondria. J. Physiol. *529*, 69–81.

Hardie, D.G. (2011). AMP-activated protein kinase: an energy sensor that regulates all aspects of cell function. Genes Dev. *25*, 1895–1908.

Hardie, D.G. (2015). AMPK: positive and negative regulation, and its role in whole-body energy homeostasis. Curr. Opin. Cell Biol. *33*, 1–7.

Hardie, D.G., Ross, F.A., and Hawley, S.A. (2012). AMPK: a nutrient and energy sensor that maintains energy homeostasis. Nat. Rev. Mol. Cell Biol. *13*, 251–262.

Hawkins, B.J., Irrinki, K.M., Mallilankaraman, K., Lien, Y.C., Wang, Y., Bhanumathy, C.D., Subbiah, R., Ritchie, M.F., Soboloff, J., Baba, Y., et al. (2010). S-glutathionylation activates STIM1 and alters mitochondrial homeostasis. J. Cell Biol. *190*, 391–405.

Hawley, S.A., Gadalla, A.E., Olsen, G.S., and Hardie, D.G. (2002). The antidiabetic drug metformin activates the AMP-activated protein kinase cascade via an adenine nucleotide-independent mechanism. Diabetes *51*, 2420–2425.

Hawley, S.A., Pan, D.A., Mustard, K.J., Ross, L., Bain, J., Edelman, A.M., Fren-guelli, B.G., and Hardie, D.G. (2005). Calmodulin-dependent protein kinase-β is an alternative upstream kinase for AMP-activated protein kinase. Cell Metab. 2, 9–19.

Hoffman, N.E., Chandramoorthy, H.C., Shamugapriya, S., Zhang, X., Rajan, S., Mallilankaraman, K., Gandhirajan, R.K., Vagnozzi, R.J., Ferrer, L.M., Sreek-rishnanilayam, K., et al. (2013). MICU1 motifs define mitochondrial calcium uni-porter binding and activity. Cell Rep. 5, 1576–1588.

Howell, J.J., Hellberg, K., Turner, M., Talbott, G., Kolar, M.J., Ross, D.S., Hox-haj, G., Saghatelian, A., Shaw, R.J., and Manning, B.D. (2017). Metformin In-hibits Hepatic mTORC1 Signaling via Dose-Dependent Mechanisms Involving AMPK and the TSC Complex. Cell Metab. 25, 463–471.

Hurley, R.L., Anderson, K.A., Franzone, J.M., Kemp, B.E., Means, A.R., and Witters, L.A. (2005). The Ca2+/calmodulin-dependent protein kinase kinases are AMP-activated protein kinase kinases. J. Biol. Chem. 280, 29060–29066.

Izzo, V., Bravo-San Pedro, J.M., Sica, V., Kroemer, G., and Galluzzi, L. (2016). Mitochondrial Permeability Transition: New Findings and Persisting Uncer-tainties. Trends Cell Biol. 26, 655–667.

Joiner, M.L., Koval, O.M., Li, J., He, B.J., Allamargot, C., Gao, Z., Luczak, E.D., Hall, D.D., Fink, B.D., Chen, B., et al. (2012). CaMKII determines mitochondrial stress responses in heart. Nature 491, 269–273.

Kahn, B.B., Alquier, T., Carling, D., and Hardie, D.G. (2005). AMP-activated protein kinase: ancient energy gauge provides clues to modern understanding of metabolism. Cell Metab. 1, 15–25.

Kamer, K.J., and Mootha, V.K. (2014). MICU1 and MICU2 play nonredundant roles in the regulation of the mitochondrial calcium uniporter. EMBO Rep. 15, 299–307.

King, J.D., Jr., Fitch, A.C., Lee, J.K., McCane, J.E., Mak, D.O., Foskett, J.K., and Hallows, K.R. (2009). AMP-activated protein kinase phosphorylation of the R domain inhibits PKA stimulation of CFTR. Am. J. Physiol. Cell Physiol. 297, C94–C101.

Kirichok, Y., Krapivinsky, G., and Clapham, D.E. (2004). The mitochondrial cal-cium uniporter is a highly selective ion channel. Nature 427, 360–364.

Kuznetsov, A.V., Usson, Y., Leverve, X., and Margreiter, R. (2004). Subcellular heterogeneity of mitochondrial function and dysfunction: evidence obtained by confocal imaging. Mol. Cell. Biochem. 256-257, 359–365.

Kwong, J.Q., Lu, X., Correll, R.N., Schwanekamp, J.A., Vagnozzi, R.J., Sar-gent, M.A., York, A.J., Zhang, J., Bers, D.M., and Molkentin, J.D. (2015). The Mitochondrial Calcium Uniporter Selectively Matches Metabolic Output to Acute Contractile Stress in the Heart. Cell Rep. 12, 15–22.

Lee, J.H., So, J.H., Jeon, J.H., Choi, E.B., Lee, Y.R., Chang, Y.T., Kim, C.H., Bae, M.A., and Ahn, J.H. (2011). Synthesis of a new fluorescent small molecule probe and its use for in vivo lipid imaging. Chem. Commun. (Camb.) 47, 7500–7502.

Li, W.C., Ralphs, K.L., and Tosh, D. (2010). Isolation and culture of adult mouse hepatocytes. Methods Mol. Biol 633, 185–196.

Li, Y., Xu, S., Mihaylova, M.M., Zheng, B., Hou, X., Jiang, B., Park, O., Luo, Z., Lefai, E., Shyy, J.Y., et al. (2011). AMPK phosphorylates and inhibits SREBP activity to attenuate hepatic steatosis and atherosclerosis in diet-induced in-sulin-resistant mice. Cell Metab. 13, 376–388.

Liu, J.C., Parks, R.J., Liu, J., Stares, J., Rovira, I.I., Murphy, E., and Finkel, T. (2017). The In Vivo Biology of the Mitochondrial Calcium Uniporter. Adv. Exp. Med. Biol. 982, 49–63.

Luongo, T.S., Lambert, J.P., Yuan, A., Zhang, X., Gross, P., Song, J., Shan-mughapriya, S., Gao, E., Jain, M., Houser, S.R., et al. (2015). The Mitochondrial Calcium Uniporter Matches Energetic Supply with Cardiac Workload during Stress and Modulates Permeability Transition. Cell Rep. 12, 23–34.

Madiraju, A.K., Erion, D.M., Rahimi, Y., Zhang, X.M., Braddock, D.T., Albright, R.A., Prigaro, B.J., Wood, J.L., Bhanot, S., MacDonald, M.J., et al. (2014). Met-formin suppresses gluconeogenesis by inhibiting mitochondrial glycerophos-phate dehydrogenase. Nature 510, 542–546.

Mallilankaraman, K., Cárdenas, C., Doonan, P.J., Chandramoorthy, H.C., Irrinki, K.M., Golenár, T., Csordás, G., Madireddi, P., Yang, J., Müller, M.,

et al. (2012a). MCUR1 is an essential component of mitochondrial Ca2+ up-take that regulates cellular metabolism. Nat. Cell Biol. 14, 1336–1343.

Mallilankaraman, K., Doonan, P., Cárdenas, C., Chandramoorthy, H.C., Müller, M., Miller, R., Hoffman, N.E., Gandhirajan, R.K., Molgó, J., Birnbaum, M.J., et al. (2012b). MICU1 is an essential gatekeeper for MCU-mediated mitochon-drial Ca(2+) uptake that regulates cell survival. Cell 151, 630–644.

Mayes, P.A., and Felts, J.M. (1967). Regulation of fat metabolism of the liver. Nature 215, 716–718.

Mihaylova, M.M., and Shaw, R.J. (2011). The AMPK signalling pathway coor-dinates cell growth, autophagy and metabolism. Nat. Cell Biol. 13, 1016–1023.

Mukhopadhyay, P., Rajesh, M., Haskó, G., Hawkins, B.J., Madesh, M., and Pacher, P. (2007). Simultaneous detection of apoptosis and mitochondrial su-peroxide production in live cells by flow cytometry and confocal microscopy. Nat. Protoc. 2, 2295–2301.

Nemani, N., Carvalho, E., Tomar, D., Dong, Z., Ketschek, A., Breves, S.L., Jaña, F., Worth, A.M., Heffler, J., Palaniappan, P., et al. (2018). MIRO-1 Deter-mines Mitochondrial Shape Transition upon GPCR Activation and Ca2+ Stress. Cell Rep. 23, 1005–1019.

Pacher, P., Csordás, P., Schneider, T., and Hajnóczky, G. (2000). Quantifica-tion of calcium signal transmission from sarco-endoplasmic reticulum to the mitochondria. J. Physiol. 529, 553–564.

Paillard, M., Csordás, G., Szanda, G., Golenár, T., Debattisti, V., Bartok, A., Wang, N., Moffat, C., Seifert, E.L., Spät, A., and Hajnóczky, G. (2017). Tissue-Specific Mitochondrial Decoding of Cytoplasmic Ca2+ Signals Is Controlled by the Stoichiometry of MICU1/2 and MCU. Cell Rep. 18, 2291–2300.

Pan, X., Liu, J., Nguyen, T., Liu, C., Sun, J., Teng, Y., Fergusson, M.M., Rovira, I.I., Allen, M., Springer, D.A., et al. (2013). The physiological role of mitochon-drial calcium revealed by mice lacking the mitochondrial calcium uniporter. Nat. Cell Biol. 15, 1464–1472.

Patron, M., Checchetto, V., Raffaello, A., Teardo, E., Vecellio Reane, D., Man-toan, M., Granatiero, V., Szabò, I., De Stefani, D., and Rizzuto, R. (2014). MICU1 and MICU2 finely tune the mitochondrial Ca2+ uniporter by exerting opposite effects on MCU activity. Mol. Cell 53, 726–737.

Payne, R., Hoff, H., Roskowski, A., and Foskett, J.K. (2017). MICU2 Restricts Spatial Crosstalk between InsP3R and MCU Channels by Regulating Threshold and Gain of MICU1-Mediated Inhibition and Activation of MCU. Cell Rep. 21, 3141–3154.

Perocchi, F., Gohil, V.M., Girgis, H.S., Bao, X.R., McCombs, J.E., Palmer, A.E., and Mootha, V.K. (2010). MICU1 encodes a mitochondrial EF hand protein required for Ca(2+) uptake. Nature 467, 291–296.

Perry, R.J., Samuel, V.T., Petersen, K.F., and Shulman, G.I. (2014). The role of hepatic lipids in hepatic insulin resistance and type 2 diabetes. Nature 510, 84–91.

Petersen, M.C., Vatner, D.F., and Shulman, G.I. (2017). Regulation of hepatic glucose metabolism in health and disease. Nat. Rev. Endocrinol. 13, 572–587.

Plovanich, M., Bogorad, R.L., Sancak, Y., Kamer, K.J., Strittmatter, L., Li, A.A., Girgis, H.S., Kuchimanchi, S., De Groot, J., Speciner, L., et al. (2013). MICU2, a paralog of MICU1, resides within the mitochondrial uniporter complex to regu-late calcium handling. PLoS ONE 8, e55785.

Raffaello, A., De Stefani, D., Sabbadin, D., Teardo, E., Merli, G., Picard, A., Checchetto, V., Moro, S., Szabò, I., and Rizzuto, R. (2013). The mitochondrial calcium uniporter is a multimer that can include a dominant-negative pore-forming subunit. EMBO J. 32, 2362–2376.

Sancak, Y., Markhard, A.L., Kitami, T., Kovács-Bogdán, E., Kamer, K.J., Ude-shi, N.D., Carr, S.A., Chaudhuri, D., Clapham, D.E., Li, A.A., et al. (2013). EMRE is an essential component of the mitochondrial calcium uniporter complex. Science 342, 1379–1382.

Shanmughapriya, S., Rajan, S., Hoffman, N.E., Higgins, A.M., Tomar, D., Nem-ani, N., Hines, K.J., Smith, D.J., Eguchi, A., Vallem, S., et al. (2015a). SPG7 Is an Essential and Conserved Component of the Mitochondrial Permeability Transition Pore. Mol. Cell 60, 47–62.

Shanmughapriya, S., Rajan, S., Hoffman, N.E., Zhang, X., Guo, S., Kolesar, J.E., Hines, K.J., Ragheb, J., Jog, N.R., Caricchio, R., et al. (2015b). Ca2+

signals regulate mitochondrial metabolism by stimulating CREB-mediated expression of the mitochondrial Ca2+ uniporter gene MCU. Sci. Signal. 8, ra23.

Shaw, R.J., Lamia, K.A., Vasquez, D., Koo, S.H., Bardeesy, N., Depinho, R.A., Montminy, M., and Cantley, L.C. (2005). The kinase LKB1 mediates glucose homeostasis in liver and therapeutic effects of metformin. Science 310, 1642–1646.

Shui, J.W., Hu, M.C., and Tan, T.H. (2007). Conditional knockout mice reveal an essential role of protein phosphatase 4 in thymocyte development and pre-T-cell receptor signaling. Mol. Cell. Biol. 27, 79–91.

Tomar, D., Dong, Z., Shanmughapriya, S., Koch, D.A., Thomas, T., Hoffman, N.E., Timbalia, S.A., Goldman, S.J., Breves, S.L., Corbally, D.P., et al. (2016). MCUR1 Is a Scaffold Factor for the MCU Complex Function and Promotes Mitochondrial Bioenergetics. Cell Rep. 15, 1673–1685.

van den Berghe, G. (1991). The role of the liver in metabolic homeostasis: implications for inborn errors of metabolism. J. Inherit. Metab. Dis. 14, 407–420.

Weibel, E.R., Stäubli, W., Gnägi, H.R., and Hess, F.A. (1969). Correlated morphometric and biochemical studies on the liver cell. I. Morphometric model, stereologic methods, and normal morphometric data for rat liver. J. Cell Biol. 42, 68–91.

White, C., Li, C., Yang, J., Petrenko, N.B., Madesh, M., Thompson, C.B., and Foskett, J.K. (2005). The endoplasmic reticulum gateway to apoptosis by Bcl-X(L) modulation of the InsP3R. Nat. Cell Biol. 7, 1021–1028.

Woods, A., Johnstone, S.R., Dickerson, K., Leiper, F.C., Fryer, L.G.D., Neumann, D., Schlattner, U., Wallimann, T., Carlson, M., and Carling, D. (2003). LKB1 is the upstream kinase in the AMP-activated protein kinase cascade. Curr. Biol. 13, 2004–2008.

Zhou, G., Myers, R., Li, Y., Chen, Y., Shen, X., Fenyk-Melody, J., Wu, M., Ventre, J., Doebber, T., Fujii, N., et al. (2001). Role of AMP-activated protein kinase in mechanism of metformin action. J. Clin. Invest. 108, 1167–1174.

STAR★METHODS

KEY RESOURCES TABLE

REAGENT or RESOURCE	SOURCE	IDENTIFIER
Antibodies		
Rabbit Polyclonal anti- ACC	Cell Signaling Technology	Cat# 3662
Rabbit Polyclonal anti- AMPKα	Cell Signaling Technology	Cat# 2532
Rabbit Polyclonal anti- ATF-6α	Santa Cruz Biotechnology Inc.	Cat# sc-166659
Mouse monoclonal anti- ATP5A	Abcam	Cat# ab14748
Rabbit monoclonal anti- CaMKII-α (D10C11)	Cell Signaling Technology	Cat# 11945
Rabbit Polyclonal anti- Carnitine Palmitoyl Transferase-1	Alpha Diagnostic Intl. Inc.	Cat# CPT1M11-A
Mouse monoclonal anti- ERK1/ERK2	Thermo Scientific Pierce	Cat# MA5-15605
Rabbit monoclonal anti- Fatty Acid Synthase (C20G5)	Cell Signaling Technology	Cat# 3180
Mouse monoclonal anti- FLAG M2-Peroxidase (HRP)	Sigma-Aldrich	Cat# A8592-1MG
Mouse monoclonal anti- FLAG M2	Sigma-Aldrich	Cat# F1804-1MG
Rat monoclonal anti- HA-Peroxidase	Sigma-Aldrich	Cat# 12013819001
Rabbit monoclonal anti- LKB1 (D60C5)	Cell Signaling Technology	Cat# 3047
Rabbit Polyclonal anti- MCU	Sigma-Aldrich	Cat# HPA016480
Rabbit Polyclonal anti- MCUR1	Tomar et al., 2016	N/A
Rabbit Polyclonal anti- MICU1	Tomar et al., 2016	N/A
Rabbit Polyclonal anti- mtTFA	Abcam	Cat# ab138351
Rabbit Polyclonal anti- NRF1	Cell Signaling Technology	Cat# 12381
Mouse monoclonal Total OXPHOS Rodent WB Antibody Cocktail	Abcam	Cat# ab110413
Rabbit Polyclonal anti- Phospho- ACC (Ser79)	Cell Signaling Technology	Cat# 3661
Rabbit Polyclonal anti- Phospho-AMPKα (Thr172)	Cell Signaling Technology	Cat# 2531
Rabbit monoclonal anti- Phospho-CaMKII (Thr286) (D21E4)	Cell Signaling Technology	Cat# 12716S
Rabbit Polyclonal anti- Phospho-p44/42 MAPK (Erk1/2) (Thr202/Tyr204)	Cell Signaling Technology	Cat# 9101
Rabbit monoclonal anti- Phospho-PERK (Thr980) (16F8)	Cell Signaling Technology	Cat# 3179
Rabbit Polyclonal anti- PGC1 alpha	Abcam	Cat# ab54481
Mouse monoclonal anti- PPX (C-6)	Santa Cruz Biotechnology Inc.	Cat# sc-374106
Rabbit Polyclonal anti- SREBP-1 (C-20)	Santa Cruz Biotechnology Inc.	Cat# sc-366
Rabbit Polyclonal anti- Tom20 (FL-145)	Santa Cruz Biotechnology Inc.	Cat# sc11415
Rabbit monoclonal anti- XBP-1 s (D2C1F)	Cell Signaling Technology	Cat# 12782
Mouse monoclonal anti- β-Actin (C4)	Santa Cruz Biotechnology Inc.	Cat# sc47778
Goat anti-Mouse IgG (H+L)-HRP Conjugate	Bio-Rad Laboratories	Cat# 1721011
Goat anti-rabbit IgG, HRP-linked	Cell Signaling Technology	Cat# 7074S
Chemicals, Peptides, and Recombinant Proteins		
Acetonitrile	Sigma-Aldrich	Cat# 271004
Ammonium formate	Sigma-Aldrich	Cat# 516961
Antibiotic-antimycotic solution	Thermo Fisher Scientific	Cat# 15240112
Antimycin A	Sigma-Aldrich	Cat# A8674
BAPTA-AM	Thermo Fisher Scientific	Cat# B6769
Bis-Tris polyacrylamide gel (4-12%)	Thermo Fisher Scientific	Cat# WG1402BOX
BODIPY® 493/503	Thermo Fisher Scientific	Cat# D3922

(Continued on next page)

REAGENT or RESOURCE	SOURCE	IDENTIFIER
$CaCl_2$	Sigma-Aldrich	Cat# 21115
Cacodylate buffer	Electron Microscopy Sciences	Cat# 11652
CGP37157	Sigma-Aldrich	Cat# C8874
Chloroform	Sigma-Aldrich	Cat# CX1055
Collagenase D	Sigma-Aldrich	Cat# 11088866001
Digitonin	Sigma-Aldrich	Cat# D141
Dihydrorhodamine 123	Thermo Fisher Scientific	Cat# D632
DPBS Ca^{2+}/Mg^{2+} free	Thermo Fisher Scientific	Cat# 14190136
DPBS with Ca^{2+}/Mg^{2+}	Thermo Fisher Scientific	Cat# 14040117
Dulbecco's modified Eagle's medium (DMEM)	Thermo Fisher Scientific	Cat# 11885092
Earle's Balanced Salt Solution (EBSS)	Thermo Fisher Scientific	Cat# 24010043
EDTA	Thermo Fisher Scientific	Cat# AM9260G
EGTA	Sigma-Aldrich	Cat# 03777
Etomoxir	Sigma-Aldrich	Cat# 236020
FCCP	Sigma-Aldrich	Cat# C2920
Fetal bovine serum	HyClone-GE	Cat# SH30071.04
Formic acid	Sigma-Aldrich	Cat# 33015
Fura-FF	Sigma-Aldrich	Cat# 17085
Glucose	Sigma-Aldrich	Cat# G8644-100ML
Glucagon	Sigma-Aldrich	Cat# G2044
Glutaraldehyde	Electron Microscopy Sciences	Cat# 16020
HEPES	Thermo Fisher Scientific	Cat# 15630080
Ionomycin	Thermo Fisher Scientific	Cat# I24222
JC-1	Thermo Fisher Scientific	Cat# T3168
KCl	Sigma-Aldrich	Cat# P9333
KH_2PO_4	Sigma-Aldrich	Cat# P5655
L-glutamine	Thermo Fisher Scientific	Cat# 25030164
$MgCl_2$	Sigma-Aldrich	Cat# 449172
MitoSOX Red	Thermo Fisher Scientific	Cat# M36008
NaCl	Sigma-Aldrich	Cat# 746398
Non-essential amino acids	Thermo Fisher Scientific	Cat# 11140050
Oil Red O	Sigma-Aldrich	Cat# O0625
Oligomycin	Sigma-Aldrich	Cat# 75351
Paraformaldehyde	Electron Microscopy Sciences	Cat# 15700
PhosSTOP Phosphatase Inhibitor Cocktail	Sigma-Aldrich	Cat# 4906845001
Poly-L-lysine	Sigma-Aldrich	Cat# P4707-50ML
cOmplete Protease Inhibitor Cocktail	Sigma-Aldrich	Cat# 11697498001
Rhod-2-AM	Thermo Fisher Scientific	Cat# R1245MP
RIPA buffer	EMD-Millipore	Cat# 20-188
Rotenone	Sigma-Aldrich	Cat# 557368
Ru360	Sigma-Aldrich	Cat# 557440
Sodium gluconate	Sigma-Aldrich	Cat# S2054
Sucrose	Sigma-Aldrich	Cat# 84097
Tetramethylrhodamine methyl ester	Thermo Fisher Scientific	Cat# T668
Thapsigargin	Thermo Fisher Scientific	Cat# T7458
Tricaine	Sigma-Aldrich	Cat# E10521
Vasopressin	Sigma-Aldrich	Cat# 1711100
William's E medium	Thermo Fisher Scientific	Cat# 32551020

REAGENT or RESOURCE	SOURCE	IDENTIFIER
Critical Commercial Assays		
Pierce™ 660nm Protein Assay	Thermo Fisher Scientific	Cat# 22662
CellTiter-Glo Assay	Promega	Cat# G7571
AMP Glo Assay	Promega	Cat# V5011
ALT Activity Assay	Sigma-Aldrich	Cat# MAK052
β-hydroxybutyrate Assay	Cayman	Cat# 700190
Glucose (HK) Assay Kit	Sigma-Aldrich	Cat# GAHK20
Triglyceride Assay	Cayman	Cat# 10010303
Experimental Models: Cell Lines		
HepG2	ATCC	Cat# HB-8065
Primary Mouse Hepatocytes	This Study	N/A
Experimental Models: Organisms/Strains		
C57BL/6J Mice	The Jackson Laboratory, USA	Stock#000664
MCU$^{fl/fl}$ mice	Luongo et al., 2015	N/A
B6.Cg-Tg(Alb-cre)21Mgn/J	The Jackson Laboratory, USA	Stock# 003574
MCU$^{\Delta hep}$ mice	This Study	N/A
AMPKα1/α2$^{fl/fl}$ mice	Foretz et al., 2010	N/A
AMPK α1/α2$^{\Delta hep}$ mice	This Study	N/A
MCU-C96A-KI mice	This Study	N/A
MCU-KO zebrafish	This Study	N/A
Oligonucleotides		
PP4-siRNA (Smart Pool)	Dharmacon	Cat# L-040058-02-0005
Recombinant DNA		
Ad-T172D AMPKα1 (CA-AMPK)	This Study	N/A
Ad-MCU-Flag	This Study	N/A
Ad-GCaMP6.m	This Study	N/A
pECE HA AMPKα1 AS	Addgene	Plasmid # 69831
pEBG-T172D AMPKα1	King et al., 2009	N/A
PP4-Flag	OriGene Technologies Inc.	Cat# MR204327
Software and Algorithms		
Fiji ImageJ software	Fiji ImageJ	https://fiji.sc/
Sigma Plot 11.0	Systat Software Inc.	https://systatsoftware.com/products/sigmaplot/
Zen 2010	Carl Zeiss	https://www.zeiss.com/microscopy/us/products/microscope-software/zen.html
Graphpad Prism 6	GraphPad Software	https://www.graphpad.com/scientific-software/prism/
Metaboanalyst	Xia Lab at McGill Univeristy	https://www.metaboanalyst.ca/
MarkerView software	Sciex LLC	https://sciex.com/products/software/markerview-software
Canvas 11.0	ACD Systems	https://www.canvasgfx.com/en/support/canvas-11/

CONTACT FOR REAGENT AND RESOURCE SHARING

Further information and requests for reagents may be directed to and will be fulfilled by the Lead Contact, Muniswamy Madesh (muniswamy@uthscsa.edu).

EXPERIMENTAL MODEL AND SUBJECT DETAILS

Mouse models

Hepatocyte-specific *Mcu* knockouts (MCU$^{\Delta hep}$) were generated by crossing MCU$^{fl/fl}$ mice (Luongo et al., 2015) with hepatocyte-specific Cre recombinase transgenic mice (B6.Cg-Tg(Alb-cre)21Mgn/J, The Jackson Laboratory, USA). Hepatic AMPK-KO (AMPK$^{\Delta hep}$) mice were generated by retro orbital injection of the 1×10^{11} viral particles of adenovirus associated virus 8- Cre (AAV8-Cre under the control of the TGB promoter) in the AMPKα1/α2$^{fl/fl}$ mice which have the Lox-P site on both AMPKα1 and AMPKα2 loci. Mice were allowed to rest for 2 weeks before the experiment. To generate MCU-C96A knock in mice, gRNA1, gRNA2, ssODN containing BssHII site along with Cas9 protein was microinjected in single-celled embryo and transferred to surrogate mother. Details of oligo's sequence used for C96A-KI are given in Figure S5B. The C96A-KI is confirmed by restriction fragment analysis using BssHII restriction enzyme. All mice were grouped according to same sex and age for all the experiments. For studies utilizing primary hepatocytes *in vitro*, both male and female mice were used. However, male mice were used for all *in vivo* experiments. All animal experiments were approved by Temple University's IACUC and followed AAALAC guidelines.

Zebrafish

To generate zebrafish *mcu* mutant, three different sgRNA target sequences were designed (with PAM sequences in bold, #1: GCC GGGTTTCACTTCAGAGA**TGG** (+strand), #2: GGCTGCGAAAGTGTGTAGAT**CGG** (+ strand), and #3: TGTGCCCTGATGCCTCTGT G**AGG** (- strand). sgRNAs were *in vitro* transcribed and co-injected with mRNA coding for nCas9n into 1-cell zebrafish embryos. Activity of sgRNAs was tested by loss of underlined restriction enzyme sites Hpy118I (TCNGA), Sau3AI (GATC) and EcoNI (#3, CCTN$_5$AGG). Primers mcu-F1 (TAGAGACCGTGGTATTTCAGTCTAC) and mcu-R1 (TGCACTGCACAGTGATGATCAGCA) were used for genotyping. A deletion allele *tpl124*, generated using sgRNA#2, containing a 268 base pair deletion encompassing parts of exon 1 and intron 1, was selected for further study. All Zebrafish experiments were approved by Temple University's IACUC and followed AAALAC guidelines.

Cell culture

Primary hepatocytes were grown in Williams E medium containing 1% (v/v) antibiotic-antimycotic solution (GIBCO), 1% (v/v) 200mM L-glutamine, and 1% (v/v) non-essential amino acids under standard culture condition. HepG2 cells were cultured in Dulbecco's modified Eagle's medium (DMEM)/10% FBS, supplemented with 1% (v/v) antibiotic-antimycotic solution (GIBCO) at 5% CO_2 and 37°C.

METHOD DETAILS

Isolation of mouse primary hepatocytes

Primary adult mouse hepatocytes were isolated from 10-12 week old male and female animals using a two-step collagenase perfusion technique with slight modifications (Li et al., 2010). In brief, mice liver was sequentially perfused with perfusion medium- I (DPBS containing 10mM HEPES, 0.05% w/v KCl, 5mM Glucose, 200 μM EDTA, pH 7.4) and perfusion medium-II (DPBS containing 30mM HEPES, 0.05% w/v KCL, 5mM Glucose, 1mM $CaCl_2$, pH 7.4) containing collagenase D (400 μg/ml). Liver lobes were dissected, dissociated, and crude hepatocyte preparation passed through the gauze mesh filter (100 μM diameter). The crude hepatocyte preparation was centrifuged at the speed of 50 g for 2 min to pellet down parenchymal hepatocytes. The hepatocytes were washed five times with perfusion medium-II using the above-mentioned centrifuge conditions. Following the wash, cells were plated in culture dishes in hepatocyte attachment medium (Williams E medium containing 1% (v/v) antibiotic-antimycotic solution (GIBCO), 1% (v/v) 200mM L-glutamine, 1% (v/v) non-essential amino acids, and 10% heat inactivated fetal bovine serum). The next day, attachment media was replaced with hepatocyte culture medium (Williams E medium containing 1% (v/v) antibiotic-antimycotic solution (GIBCO), 1% (v/v) 200mM L-glutamine, and 1% (v/v) non-essential amino acids).

Mitoplast I_{MCU} patch-clamp recording

Mitoplast patch-clamp recordings for I_{MCU} current were performed at 30°C as reported earlier (Chaudhuri et al., 2013; Hoffman et al., 2013; Joiner et al., 2012; Kirichok et al., 2004; Tomar et al., 2016) with slight modifications. In brief, mitoplasts isolated from hepatocytes of MCU$^{fl/fl}$ and MCU$^{\Delta hep}$ mice were bathed in a solution containing 150mM sodium gluconate, 5.4mM KCl, 5mM $CaCl_2$, and 10mM HEPES (pH 7.2). The pipette solution contained 150mM sodium gluconate, 5mM NaCl, 135mM sucrose, 10mM HEPES, and 1.5mM EGTA (pH 7.2). I_{MCU} currents were recorded using an Axon200B patch-clamp amplifier with a Digidata 1320A acquisition board (pCLAMP 10.0 software; Axon Instruments). The external/bath solution (5 mM Ca^{2+}) was chosen on the basis of previous measurements.

Measurement of mitochondrial Ca^{2+} uptake, $\Delta\Psi_m$, and mitochondrial matrix Ca^{2+}

Mitochondrial Ca^{2+} uptake and $\Delta\Psi_m$ were measured as described earlier using dual-wavelength emission fluorimeter with slight modifications (Mallilankaraman et al., 2012a; Mallilankaraman et al., 2012b; Shanmughapriya et al., 2015a; Tomar et al., 2016). Freshly isolated mouse primary hepatocytes were washed with Ca^{2+}/Mg^{2+} free DPBS (GIBCO). An equal number of cells (5x10^6 cells)

were permeabilized with 40 μg/ml digitonin in 1.5 mL of intracellular medium (ICM- 120 mM KCl, 10 mM NaCl, 1 mM KH_2PO_4, 20 mM HEPES-Tris, pH 7.2) supplemented with 2 μM thapsigargin to block the SERCA pump and 5mM succinate to energize the mitochondria. Fura-FF (0.5 μM) was loaded at 0 s time point for the measurement of extramitochondrial Ca^{2+} ($[Ca^{2+}]_{out}$). Fluorescence emissions were monitored in a multi-wavelength excitation dual-wavelength emission fluorimeter (Delta RAM, PTI). The $[Ca^{2+}]_{out}$ is shown as the ratio of Fura-FF/FA fluorescence (excitation 340 nm/380 nm) and $\Delta\Psi_m$ as the ratio of the JC-1 fluorescence of J-aggregate (570 nm excitation/595 nm emission) and monomer (490 nm excitation/535 nm emission) forms of JC-1. The $\Delta\Psi_m$ indicator, JC-1 (800 nM), a bolus of 10 μM Ca^{2+}, and the mitochondrial uncoupler, FCCP (3 μM), were added at the indicated time points with constant stirring at 37°C. To measure the mitochondrial matrix Ca^{2+}, hepatocytes were permeabilized in 40 μg/ml digitonin in 1.5 mL of intracellular medium supplemented with thapsigargin, Ru360 (1 μM, to block mitochondrial Ca^{2+} uptake), CGP37157 (1 μM, to block mitochondrial Ca^{2+} efflux), and Fura-FF (0.5 μM). Mitochondrial uncoupler, FCCP (10 μM) was added at indicated time points without adding any Ca^{2+} bolus to release the mitochondrial Ca^{2+} store.

Mitochondrial and cytosolic Ca^{2+} measurements using confocal live cell imaging system
Primary zebrafish cells were grown on Poly-L-lysine coated glass coverslips and loaded with $_mCa^{2+}$ sensor Rhod-2 (2 μM) for 45 min in extracellular media (ECM- 120mM NaCl, 5mM KCl, 1mM KH_2PO_4, 0.2mM $MgCl_2$, 0.1mM EGTA, 20mM HEPES, pH 7.4). Cells were washed and imaged in ECM using Carl Zeiss LSM510 confocal live cell imaging system using the 560 nm excitation (Ex) laser and 580 nm emission (Em) spectra is collected. Ionomycin was added at indicated time points to increase $_cCa^{2+}$ levels. For $_cCa^{2+}$ measurements, primary hepatocytes were grown on 25-mm glass coverslips and transduced with GCaMP6 encoding adenovirus. Coverslips were mounted in an open perfusion micro-incubator (PDMI-2; Harvard Apparatus) at 37°C and imaged using the Carl Zeiss LSM510 confocal live cell imaging system using the Ex-488 nm and Em-510 nm. After 1 min of baseline recording, vasopressin (100nM) or thapsigargin (2 μM) was added, and confocal images were obtained every 3 s at 488- nm excitation using a 40x oil objective. Images were analyzed and quantitated using ZEN 2010 and ImageJ software.

Mitochondrial respiration measurements
Primary hepatocytes isolated from MCU$^{fl/fl}$ and MCU$^{\Delta hep}$ mice were plated in Poly-L-lysine coated 96 well Seahorse culture plates. Oxygen consumption rate (OCR) was measured at 37°C in an XF96 extracellular flux analyzer (Seahorse Bioscience). Respiratory chain inhibitors were added sequentially at indicated time points. For the measurement of FAO coupled OCR, cells were glucose depleted overnight and treated with carnitine palmitoyl transferase-1 inhibitor Etomoxir (40 μM) for 1 hour to monitor endogenous fatty acid utilization. Exogenous palmitate is used as fatty acid substrate for the OCR measurement using XF96 extracellular flux analyzer (Seahorse Bioscience).

Cellular AMP/ATP measurement
Mouse hepatocyte and zebrafish total cellular ATP levels were measured using CellTiter-Glo luminescent assay kit (Promega, Madison, WI, USA) as per the manufacturer's protocol. AMP levels were measured using the AMP-Glo luminescent assay kit (Promega, Madison, WI, USA). Luminescence was measured using a microplate reader (Infinite M1000 PRO, Tecan).

Mitochondrial reactive oxygen species measurement
Primary hepatocytes isolated from MCU$^{fl/fl}$ and MCU$^{\Delta hep}$ mice were plated on Poly-L-lysine coated glass coverslips. Next day, cells were loaded with the mitochondrial superoxide sensitive fluorophore MitoSOX Red (Life Technologies; 2 μM) and Dihydrorhodamine 123 (Rhod123; 2.5 μg/ml) in William's E medium (without serum) at 37°C for 30 min. Cells were then washed and imaged using a Carl Zeiss 510 confocal microscope with a 40 × oil immersion objective at 561 nm as described earlier (Mukhopadhyay et al., 2007). MitoSOX fluorescence was quantified using ImageJ software and plotted as arbitrary units in Graphpad Prism 6 software.

TMRM staining for $\Delta\Psi_m$
Mouse primary hepatocytes and zebrafish primary cells were placed on Poly-L-lysine coated glass coverslips. The next day, cells were stained with Tetramethylrhodamine, methyl ester (TMRM; 50 nM) and Dihydrorhodamine 123 (Rhod123; 2.5 μg/ml) for 30 min at 37°C. Images were acquired using a Carl Zeiss 510 confocal microscope using a 40 × oil objective at excitations of 561 nm and 488 nm, respectively. Images were quantified for TMRM fluorescence using ImageJ software and plotted as arb unit in Graphpad Prism 6 software.

Metabolic assessment of mice
The metabolic status of MCU$^{fl/fl}$ and MCU$^{\Delta hep}$ male mice were assessed using a Comprehensive Laboratory Animal Monitoring System (CLAMS; Columbus Instruments, Columbus, OH) as described earlier (Tomar et al., 2016). Mice were single housed in 12 hour light/dark cycles with a normal chow diet and water *ad libitum*. Mice were allowed to acclimate for 3 days and then oxygen consumption, carbon dioxide production, food intake and locomotor activity were measured continuously for 3 days (24 hr Fed, 24 hr Fasted and 24hrs Re-fed state) at an ambient temperature of 22°C. During the fasted state, the chow diet is restricted for 24 hours. The respiratory exchange ratio is the ratio of carbon dioxide production and oxygen consumption. For the oxidation of carbohydrate six molecules of oxygen is utilized with generation of six molecules of CO_2, resulting a RER of 1.0. However, for the oxidation of one fatty acid

molecule 23 oxygen molecules are utilized with a generation of 16 CO_2 molecules, resulting in a RER of 0.7. Therefore, we can calculate the percentage of fat utilization by using following equation:

$$\% \text{ Fat Utilized} = ((1.00 - RER)/(1.00 - 0.70)) * 100$$

Animal body composition, liver/plasma biochemistry, glucose tolerance test and glucose output assay

Normal chow diet fed 10 weeks old male mice used for body fat composition analysis by nuclear magnetic resonance (NMR) and dual emission X-ray absorptiometry (DEXA) (Echo Medical Systems, Houston, TX). Enzymatic colorimetric assay was performed to monitor liver/plasma triglyceride, plasma ketones, liver glycogen, and blood glucose as described earlier (Alenghat et al., 2008; Tomar et al., 2016). For the glucose tolerance test, 12 week old male mice were fasted overnight for approximately 16 hours by transferring mice to clean cages. Next day, mouse body weight (wt) was measured and 20% (w/v) glucose solution (2g of glucose/kg body mass) was injected intraperitoneally. The blood glucose levels were measured at the indicated time points through the tail puncture using the OneTouch Ultra Glucose Meter. The glucose output assay was performed on primary hepatocytes isolated from 12-weeks old MCU$^{fl/fl}$ and MCU$^{\Delta hep}$ mice. The freshly isolated hepatocytes were maintained in Williams E medium containing 1% (v/v) antibiotic-antimycotic solution (GIBCO), 1% (v/v) 200mM L-glutamine, 1% (v/v) non-essential amino acids, and 10% heat inactivated fetal bovine serum overnight. The following day, the media was changed to glucose output media (GOM: 118 mM NaCl, 4.7 mM KCl, 1.2 mM $MgSO_4$, 1.2 mM KH_2PO_4, 1.2mM $CaCl_2$, 20mM $NaHCO_3$, 20mM HEPES pH 7.4, and BSA 0.025%) for 2h before induction of glycogenolysis. The cells were stimulated with 5nM Glucagon in GOM for 2h, and culture supernatants were collected and glucose content was measured by Glucose (HK) Assay Kit.

Lipid staining in primary hepatocytes, liver sections and whole zebrafish

Primary mice hepatocytes were isolated from MCU$^{fl/fl}$ and MCU$^{\Delta hep}$ and cultured in Poly-L-lysine coated glass coverslips with Williams E medium containing 5mM Glucose (low glucose condition) or 25mM Glucose (high glucose condition) for 24 hours. The next day, the medium for the hepatocytes was replaced with Earle's Balanced Salt Solution (EBSS) to induce starvation for 2 hours. After incubation, cells were loaded with BODIPY® 493/503 (1 μg/ml) in serum-free medium for 30 min. Cells were washed and images were acquired using a Carl Zeiss 510 confocal microscope using a 40 × oil objective at 488 nm excitation. Images were quantified for the size and number of lipid droplets using ImageJ software. For the histological evaluation of hepatic lipid accumulation, mice liver was perfused with PBS and subsequently with 4% paraformaldehyde to fix the tissue. Liver tissue was embedded in paraffin to cut the 5 μM thin tissue sections and subsequently stained for Oil Red O and hematoxylin and eosin (H&E). Histological images were acquired in bright field light microscope (Nikon, USA). Zebrafish lipid content was visualized by staining with Lipid Green. Wild-type and MCU-KO zebrafish were incubated in 100 μM of Lipid Green for 15 min (Lee et al., 2011). After incubation, zebrafish were anesthetized in tricaine containing water and *in vivo* confocal microscopy was performed using the Carl Zeiss LSM710 two-photon confocal system.

Electron microscopy to visualize hepatic ultrastructure

MCU$^{fl/fl}$ and MCU$^{\Delta hep}$ mice were anesthetized, and the liver was perfused with PBS for 2 minutes at 35°C followed by 0.15 M cacodylate buffer (Ted Pella Inc., Redding, CA) pH7.4 containing 2.5% glutaraldehyde (Electron Microscopy Sciences, Hartfield, PA), 2% formaldehyde (fresh from paraformaldehyde (EMS)) with 2mM $CaCl_2$ and 20 mM KCl at 35°C for 5 minutes. Liver lobes from the animal were removed and fixed for an additional 2-3 h on ice in the same tissue fixing solution. Liver tissue was sectioned, and images were acquired using the Zeiss LIBRA120 TEM equipped with Gatan UltraScan, 1000 2k x 2k CCD EFTEM, and energy filtering.

Immunoblotting and co-immunoprecipitation assay

Immunoblotting for the detection of protein expression and phosphorylation was performed using the equal amount of total cell lysate prepared from primary mice hepatocytes or zebrafish. Proteins were extracted from primary hepatocytes isolated from mice liver or zebrafish using RIPA buffer (50 mM Tris-HCl, pH 7.4, 150 mM NaCl, 0.25% deoxycholic acid, 1 mM EDTA, 1% NP-40 supplemented with protease inhibitor cocktail (Roche) and PhosSTOP Phosphatase Inhibitor Cocktail (Roche)). Protein concentrations were quantified using Pierce™ 660nm Protein Assay (Thermo Scientific Inc.) and equal amounts of protein were separated on 4%–12% Bis-Tris polyacrylamide gel. Proteins were transferred to a PVDF membrane, and probed with indicated antibodies. For co-immunoprecipitation, proteins were extracted from HepG2 cells transiently transfected with AMPK-HA and/or PP4-Flag using RIPA buffer. Indicated antibodies were used to pull-down the specific protein. The input (10% of total cell lysates) and immunoprecipitates were probed with specified antibody.

Global lipidomic profiling

Preparation of samples for lipidomic analysis

To monitor global lipidomics alterations in MCU$^{\Delta hep}$ mice, 12-week-old mice were used. MCU$^{\Delta hep}$ mice were fed with Metformin (1.25mg/ml metformin in drinking water) for three weeks. Mice liver were harvested and frozen in liquid nitrogen until the lipids were extracted. Liver sections were subjected to homogenization to uniformity in ice cold phosphate buffered saline (PBS) such

that a final suspension of 10% w/v liver homogenate in PBS were obtained. 50 μL of this suspension was used in the extraction and analysis of liver lipids.

Extraction of lipids from liver tissues

50 μL of liver homogenate was diluted with 150 μL of PBS. To the mixture thus obtained, a mixture of internal standards were added followed by vortexing and incubating on ice for 10 minutes for equilibration of the IS with the sample. Following incubation, 1 mL of methanol was added to the sample followed by sonication to mix the samples. Thereafter 0.5 mL of chloroform was added and the samples were sonicated again to mix the solvents to obtain a well dispersed monophasic extraction mixture. This mixture was then incubated at 48°C for one hour to optimize the extraction of highly non polar lipids. Following incubation, a phase break implemented out by the addition of 1 mL of chloroform followed by 2mL of water. The resultant mixture was vortexed for 30 s and then centrifuged at 3500 g to enable phase separation. Following centrifugation, the bottom organic layer containing the lipids was transferred to a fresh tube. The top aqueous layer was washed with an additional 1 mL of $CHCl_3$, vortexed, centrifuged and the separated organic layer was combined with the previous organic fraction. The lipid extracts thus obtained was dried via vacuum centrifugation and re-suspended in 200 μL of methanol. The re-suspended solution was incubated at 48°C for 10 minutes vortexed, and 50 μL transferred to 200 μL autosampler vials for analysis via ultra-performance liquid chromatography high resolution mass spectrometry.

Analysis of lipids by untargeted mass spectrometry

5 μL of the lipid extract prepared as detailed above was analyzed following separation on a Acquity CSH C18 reverse phase column (100Å, 3.5 μm, 3 mm X 150 mm, Waters) using a Shimadzu Nexera UPLC chromatographic system coupled to Sciex TripleTOF 5600+ quadrupole time of flight mass analyzer. Data was acquired in the positive mode in an untargeted data dependent manner in the mass range of 50-1200 Da. A 28 minute chromatographic separation utilizing a linear gradient of 60:40 acetonitrile:water with 10mM ammonium formate and 0.1% formic acid as mobile phase A and 90:10 isopropanol:acetonitrile with 10mM ammonium formate and 0.1% formic acid as mobile phase B.

Data Analysis

The acquired data was subjected to post processing via MarkerView software (Sciex LLC). Following normalization to total ion current and alignment of retention times, features were extracted as m/z retention time pairs. The extracted features were subjected statistical analysis using Metaboanalyst. The data was first subjected to log transformation followed by centering using Pareto scaling (mean-centered and divided by the square of the standard deviation of each variable). Cluster analysis was performed using Euclidean distance measure and Ward clustering algorithm. ANOVA and Tukey's HSD post hoc analysis with an FDR = 0.001 threshold was used to identify the top feature differences between the three groups. Those features identified as being significantly different were then identified via comparison against Lipidmaps database as well as the elution retention time window for that lipid class.

QUANTIFICATION AND STATISTICAL ANALYSIS

Data were expressed as the mean $\pm$ SE and statistical significance was evaluated via Student's unpaired t test, one-way and two-way ANOVA with Tukey's HSD post hoc analysis, where appropriate. $p < 0.05$ was considered statistically significant. All experiments were conducted at least three times unless specified. Replicates and statistical analysis information is reported in the figure legends. Data were plotted either with Sigma Plot 11.0 software or GraphPad Prism version 6 software.

Supplemental Information

Blockade of MCU-Mediated Ca^{2+} Uptake

Perturbs Lipid Metabolism

via PP4-Dependent AMPK Dephosphorylation

Dhanendra Tomar, Fabián Jaña, Zhiwei Dong, William J. Quinn III, Pooja Jadiya, Sarah L. Breves, Cassidy C. Daw, Subramanya Srikantan, Santhanam Shanmughapriya, Neeharika Nemani, Edmund Carvalho, Aparna Tripathi, Alison M. Worth, Xueqian Zhang, Roshanak Razmpour, Ajay Seelam, Stephen Rhode, Anuj V. Mehta, Michael Murray, Daniel Slade, Servio H. Ramirez, Prashant Mishra, Glenn S. Gerhard, Jeffrey Caplan, Luke Norton, Kumar Sharma, Sudarsan Rajan, Darius Balciunas, Dayanjan S. Wijesinghe, Rexford S. Ahima, Joseph A. Baur, and Muniswamy Madesh

Blockade of MCU-Mediated Ca^{2+} Uptake Perturbs Lipid Metabolism via PP4-Dependent AMPK Dephosphorylation

Dhanendra Tomar,[1,2] Fabián Jaña,[1,2] Zhiwei Dong,[1,2] William J. Quinn III,[3] Pooja Jadiya,[2] Sarah L Breves,[1,2] Cassidy C Daw[10], Subbramanya Srikantan[10], Santhanam Shanmughapriya,[1,2] Neeharika Nemani,[1,2] Edmund Carvalho,[1,2] Aparna Tripathi,[1,2] Alison M. Worth,[1,2] Xueqian Zhang,[2] Roshanak Razmpour,[4] Ajay Seelam,[1,2] Stephen Rhode,[1,2] Anuj V Mehta,[2,5] Michael Murray,[1,2] Daniel Slade,[1,2] Servio H. Ramirez,[4] Prashant Mishra,[6] Glenn S Gerhard,[1] Jeffrey Caplan,[7] Luke Norton[11], Kumar Sharma[10], Sudarsan Rajan,[1,2] Darius Balciunas,[5] Dayanjan S. Wijesinghe[8], Rexford S. Ahima[9], Joseph A. Baur,[3] and Muniswamy Madesh[1,2,10*]

S1
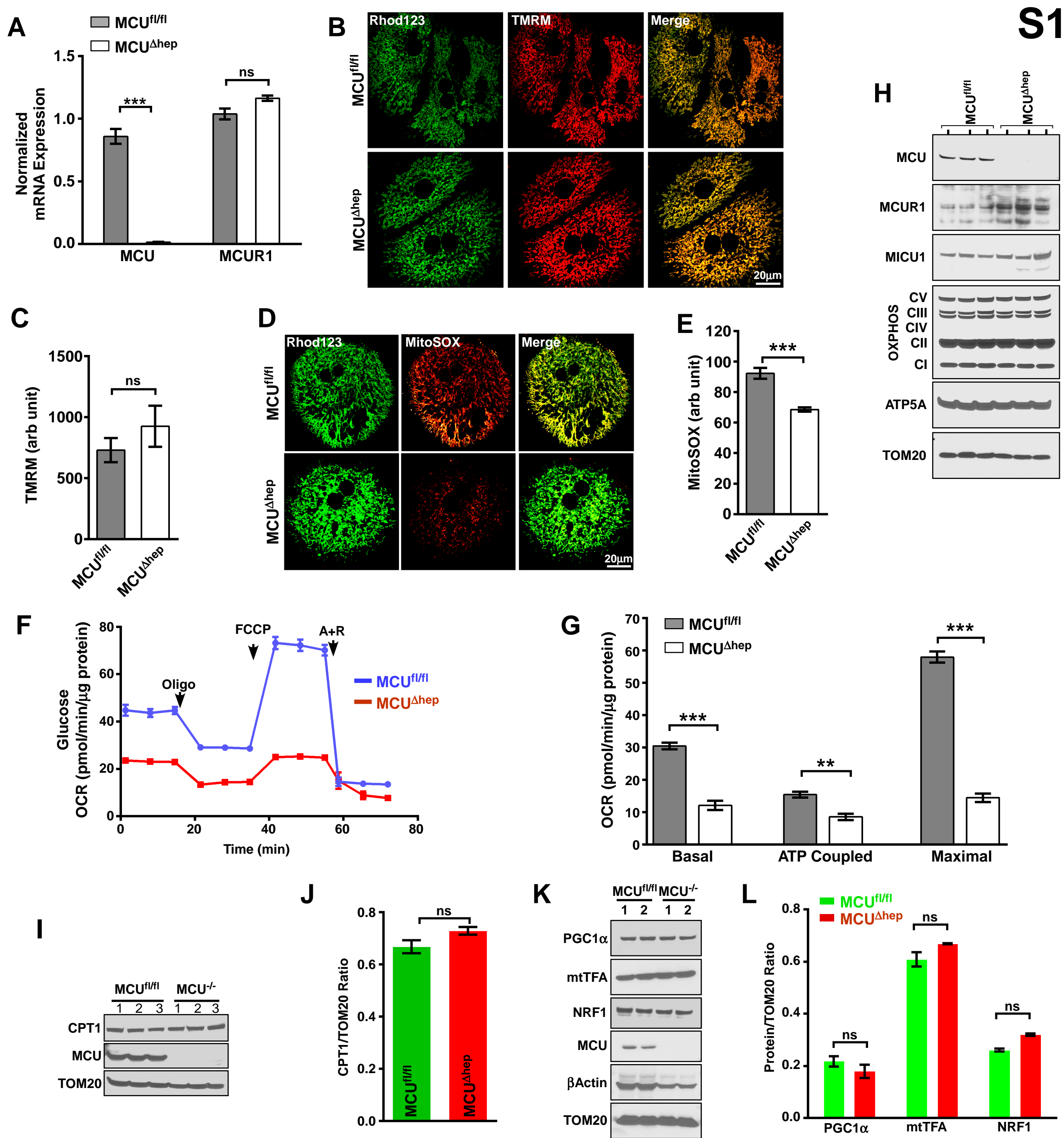
Figure S1 (Related to Figure 1): Assessment of hepatocyte-specific MCU knockout mice, mitochondrial membrane potential, oxygen consumption rate, and mitochondrial biogenesis-related proteins abundance

(A) MCU and MCUR1 mRNA abundance were quantitated in hepatocytes isolated from MCU$^{fl/fl}$ and MCU$^{\Delta hep}$ mice. Mean ± SEM; ***$p < 0.001$; ns= not significant; n = 4 mice. **(B)** MCU deletion in hepatocytes does not affect $\Delta\Psi_m$. Representative confocal images of primary hepatocytes from MCU$^{fl/fl}$ and MCU$^{\Delta hep}$ mice loaded with $\Delta\Psi_m$ indicator, TMRM (50nM). Scale bar= 20μm. n = 3 mice. **(C)** Quantification of TMRM fluorescence as an indicator of $\Delta\Psi_m$. Mean ± SEM; ns= not significant; n = 3 mice. **(D)** Elimination of MCU results in reduced mitochondrial ROS generation. Representative confocal images of primary hepatocytes from MCU$^{fl/fl}$ and MCU$^{\Delta hep}$ mice loaded with mitochondrial superoxide indicator, MitoSOX™ Red (2 μM). Scale bar= 20μm. n = 3 mice. **(E)** Quantification of MitoSOX™ Red fluorescence from raw images of Figure S1D, as an indicator of mitochondrial superoxide generation. Mean ± SEM; ***$p < 0.001$; n = 3 mice. **(F)** The mitochondrial Oxygen consumption rate (OCR). OCR was measured in MCU$^{fl/fl}$ and MCU$^{\Delta hep}$ hepatocytes using the Seahorse XF Analyzer. Mean ± SEM. n = 3 mice. **(G)** After basal OCR was recording, oligomycin, FCCP, and antimycin A + rotenone were added and ATP coupled and maximal OCR were calculated from Figure S1F. Mean ± SEM. **$p < 0.01$, and ***$p < 0.001$. n = 3 mice. **(H)** MCU-KO does not affect the expression of respiratory chain complex proteins. Western blot analysis of MCU-complex (MCU, MCUR1, MICU1) and mitochondrial respiratory chain subunits complex I (NDUFB8), complex II (SDHB), complex III (UQCRC2), complex IV (MTCO1) and ATP synthase subunit ATP5A in MCU$^{fl/fl}$ and MCU$^{\Delta hep}$ hepatocytes. TOM20 was used as a loading control. n = 3 mice. **(I)** CPT1 protein expression in MCU$^{\Delta hep}$ hepatocytes. Hepatocytes isolated from MCU$^{fl/fl}$ and MCU$^{\Delta hep}$ mice were lysed in RIPA buffer and probed with indicated antibodies. n= 3 mice. **(J)** Bar graph represents densitometric analysis of CPT1 protein abundance. Data represented as mean ± SEM. ns= non-significant p value. n= 3 mice. **(K)** MCU-KO does not have any effect on mitochondrial biogenesis-regulating transcription factors. Hepatocytes isolated from 10-12 week old MCU$^{fl/fl}$ and MCU$^{\Delta hep}$ mice were lysed in RIPA buffer and probed with indicated antibodies. n= 4. **(L)** Bar graph represents densitometric analysis of mitochondrial biogenesis-regulating transcription factors protein abundance. Mean ± SEM. ns= non-significant. n= 4.
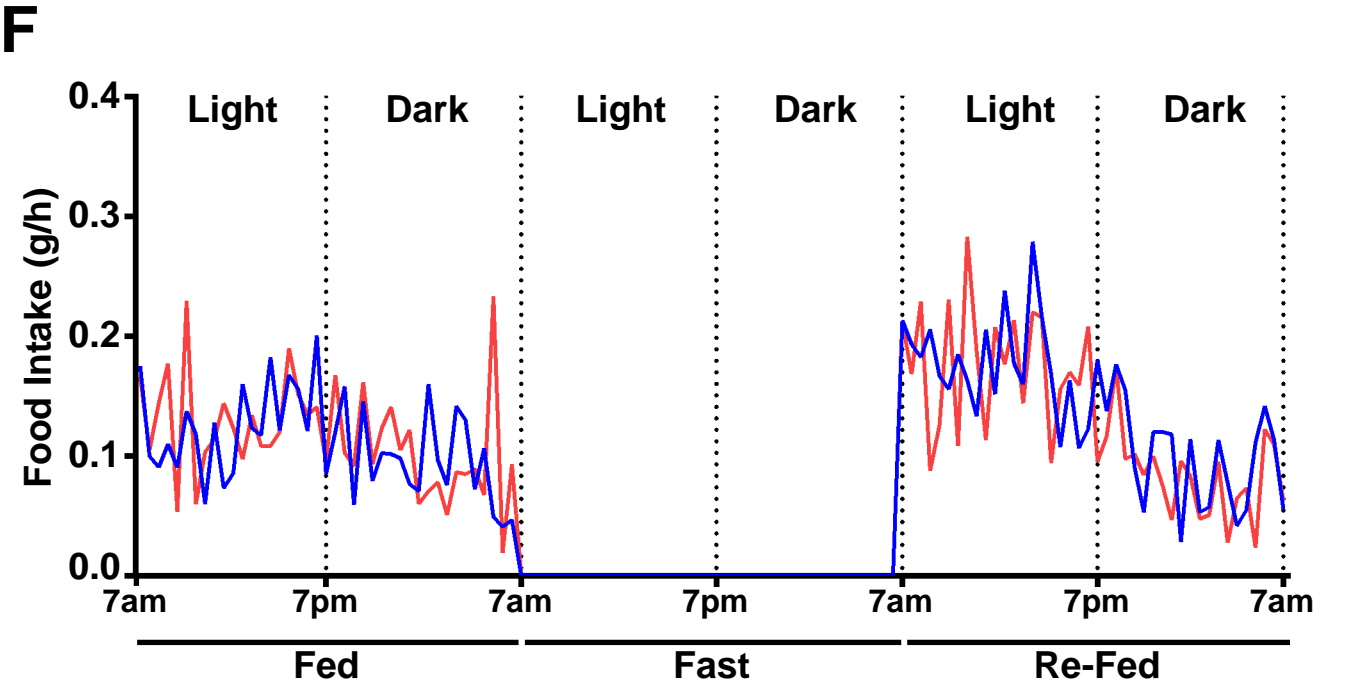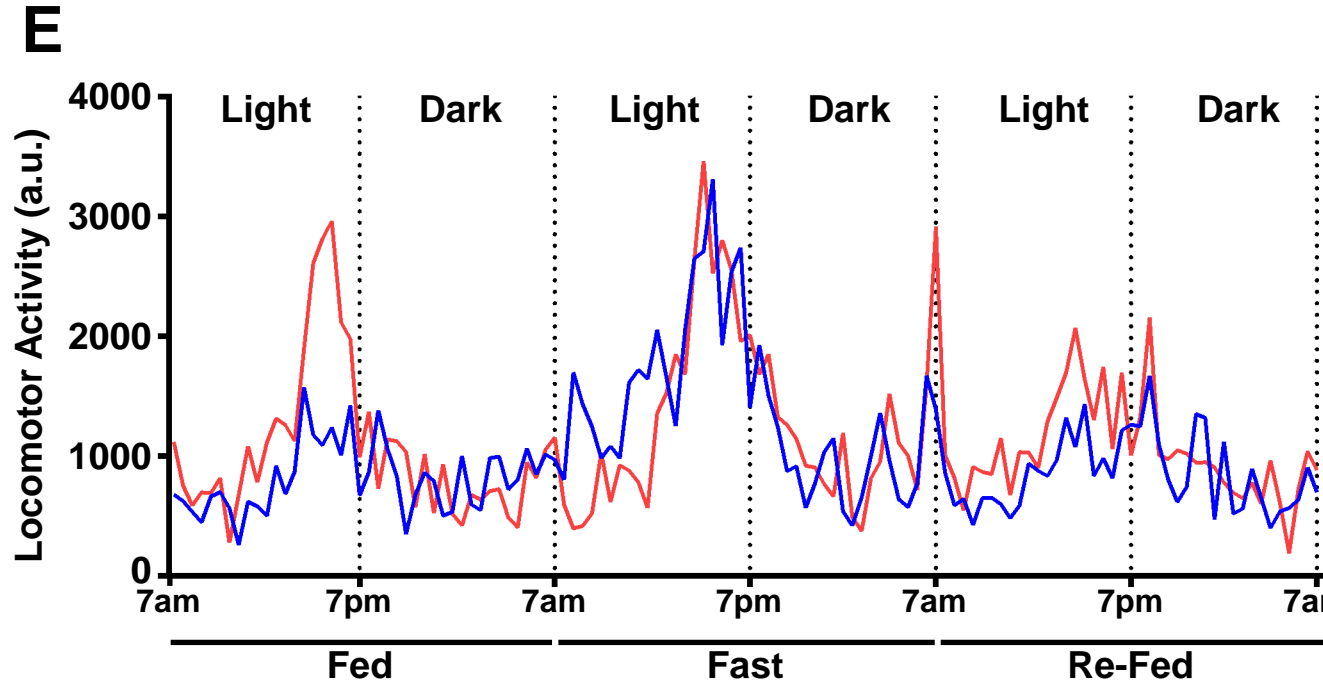
Figure S2. Metabolic phenotyping of MCU$^{fl/fl}$ and MCU$^{\Delta hep}$ mice across Fed, Fast, and Re-Fed conditions. (A) Oxygen Consumption (mL/h), (B) Respiratory Exchange Ratio, (C) %Fat Utilized, (D) Heat (kcal/hr), (E) Locomotor Activity (a.u.), and (F) Food Intake (g/h).
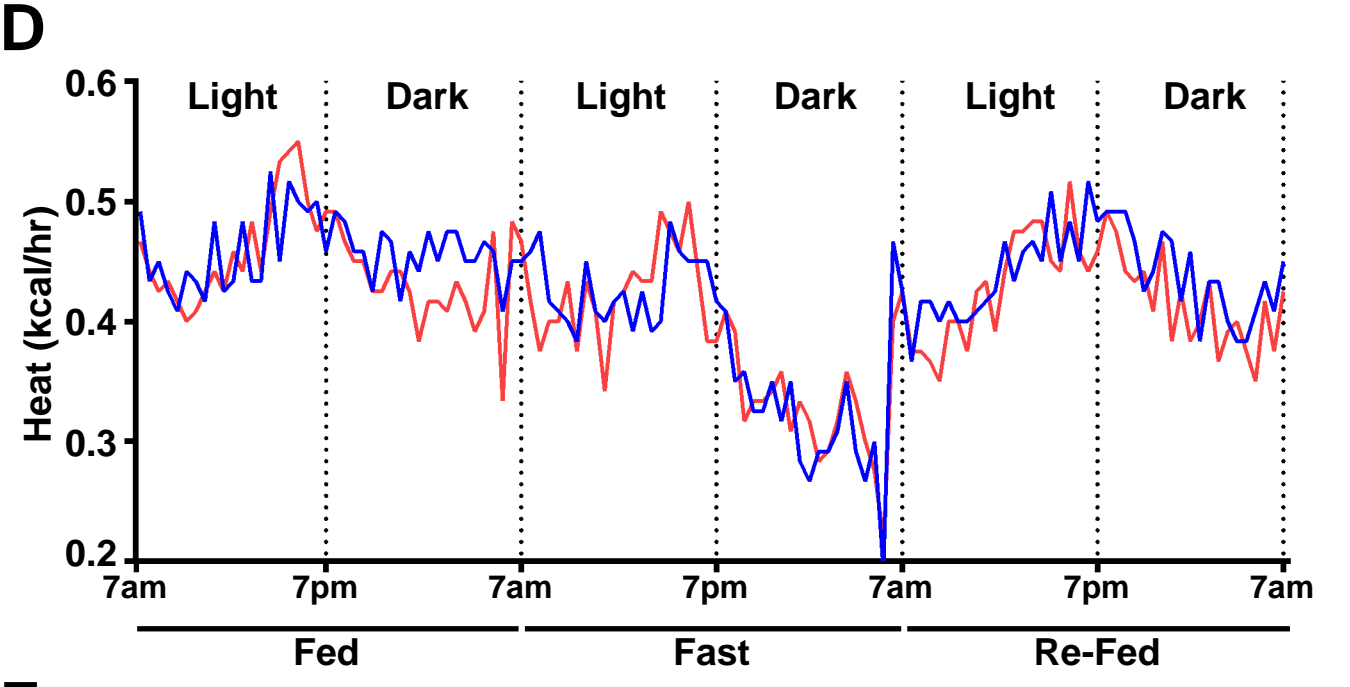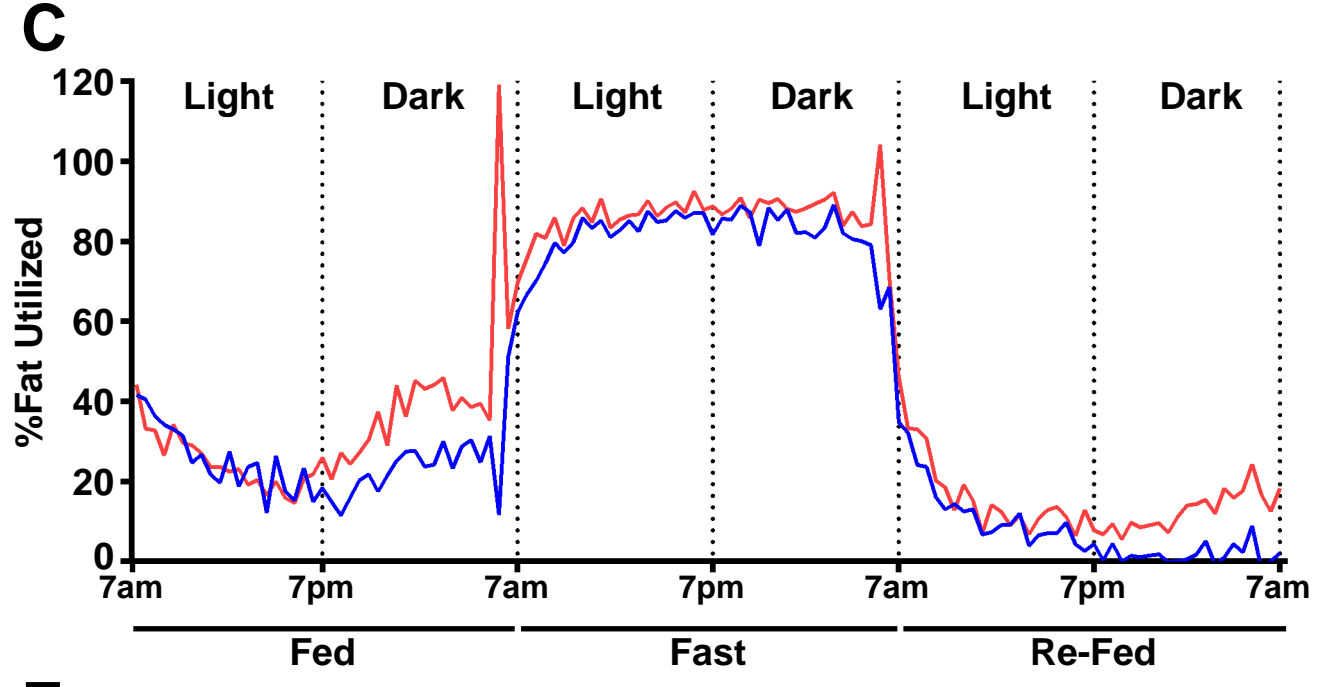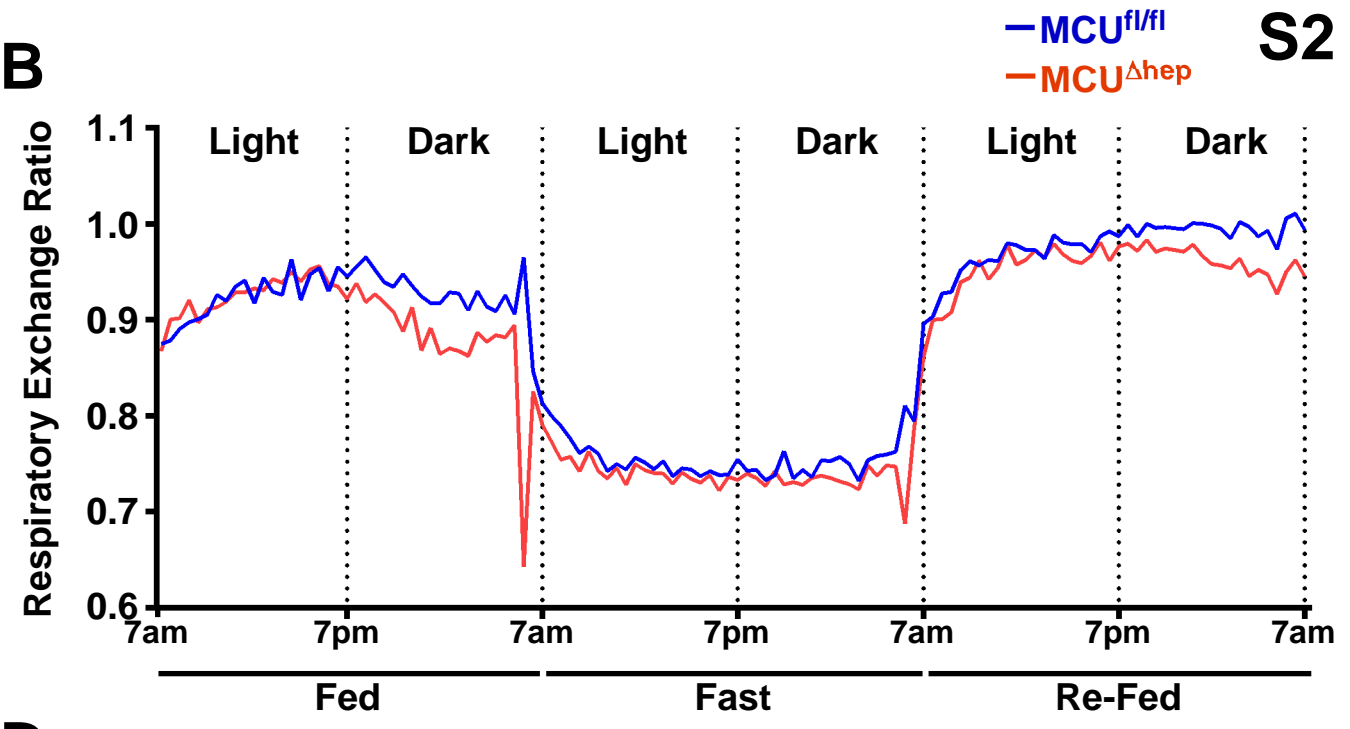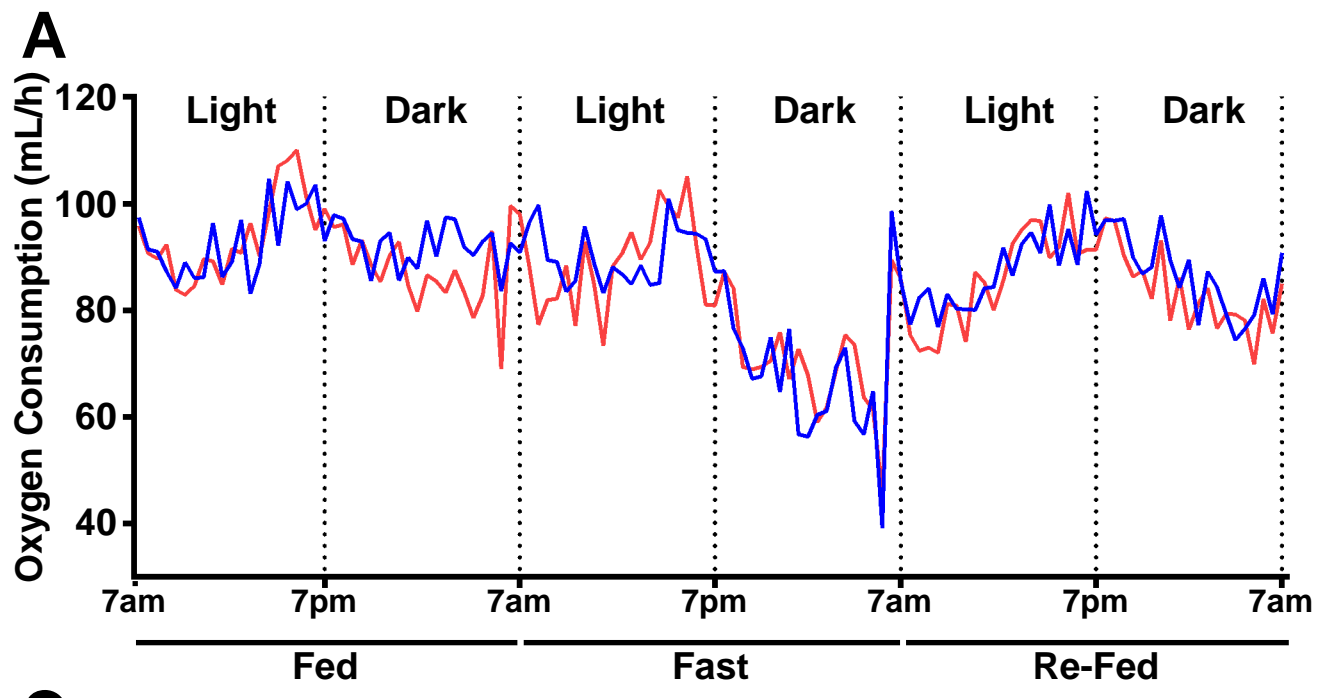
Figure S2 (Related to Figure 1): Assessment of the metabolic profiles of the mice.

(A-F) MCU$^{fl/fl}$ and MCU$^{\Delta hep}$ mice 8-10 weeks old were fed a normal chow diet and studied in a Comprehensive Animal Monitoring System (CLAMS, Columbus Instruments, Columbus, OH). **(A)** Oxygen consumption, **(B)** respiratory exchange ratio, **(C)** %Fat utilized, **(D)** Heat generated, **(E)** locomotor activity, and **(F)** food intake were measured (n = 10-12 mice per group).
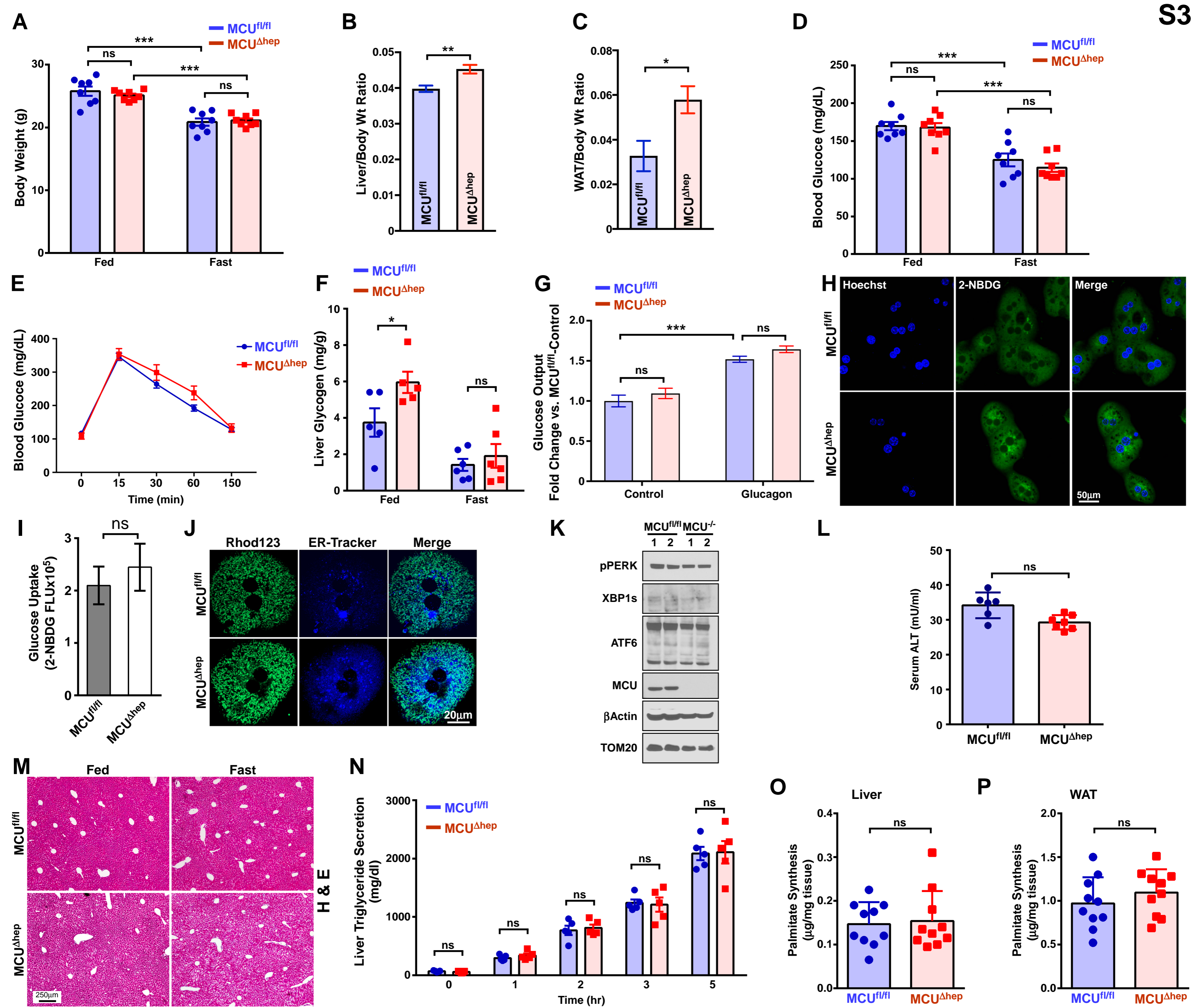
Figure S3 (Related to Figure 2): Body weight, glucose/glycogen measurements, liver injury assay, liver H&E staining, ER distribution and ER stress, liver TAG secretion, and de novo lipogenesis.

(A) Loss of MCU in hepatic tissue does not alter the gross body weight. Nuclear Magnetic Resonance (NMR) and Dual-Energy X-ray absorptiometry (DEXA) are used for the assessment of 8-week-old MCU$^{fl/fl}$ and MCU$^{\Delta hep}$ mice body composition. Mice were fed a normal chow diet and fasted for 24 hours. Body mass was monitored using NMR before and after fasting. Mean ± SEM. ***p < 0.001, ns= non-significant p value; n = 8 mice per group. **(B and C)** MCU$^{\Delta hep}$ mice demonstrate significantly increased liver/body wt and WAT/body wt ratio as compared to the MCU$^{fl/fl}$ mice. The body weight of 8-week old mice was measured, and then liver lobes and WAT was excised for quantification of tissue weights, plotted as tissue/total body wt ratio. Mean ± SEM. **p < 0.01, and *p < 0.05. n = 5-11 mice. **(D)** Blood glucose levels were unchanged in MCU$^{\Delta hep}$ mice. Tail blood was drawn from 8-week-old MCU$^{fl/fl}$ and MCU$^{\Delta hep}$ mice that were fed a normal chow diet and allowed to fast for 24 hours. Blood glucose was measured by an OneTouch Ultra glucometer. Mean ± SEM. ***p < 0.001, ns= non-significant p value; n = 8 mice per group. **(E)** Loss of *Mcu* does not alter glucose tolerance in mice. The glucose tolerance test was performed as described in the methods section. n = 10 mice per group. **(F)** Hepatic deletion of MCU leads to increased glycogen content in the liver during fed state. Liver tissue collected from fed and 24 hours fasted mice were used for the estimation of liver glycogen using enzymatic assay. Mean ± SEM. *p < 0.05, ns= non-significant p value; n = 5-6 mice per group. **(G)** Loss of *Mcu* does not alter hepatocyte glucose output. The glucose output assay was performed on primary hepatocytes in response to glucagon, and plotted as fold change compared to the MCU$^{fl/fl}$ hepatocytes. Mean ± SEM; ***p < 0.001, ns= not significant. **(H)** MCU-KO in hepatocytes does not affect hepatic glucose uptake. Glucose uptake was visualized by confocal microscope after culturing the hepatocytes from MCU$^{fl/fl}$ and MCU$^{\Delta hep}$ mice with 2-NBDG instead of glucose. Hoechst stain was used to visualize nuclei. n= 3 mice. **(I)** Bar graph for the quantification of 2-NBDG fluorescence as an indicator of glucose uptake. Mean ± SEM; ns= not significant. n= 3 mice. **(J)** MCU-KO does not affect endoplasmic reticulum distribution. Hepatocytes isolated from MCU$^{fl/fl}$ and MCU$^{\Delta hep}$ mice were stained with Rhod123 and ER-tracker Blue. Distribution of mitochondria and ER was visualized by confocal imaging. n= 3. **(K)** Loss of MCU in hepatocytes does not show altered ER-stress. Hepatocytes isolated from 10-12 week old MCU$^{fl/fl}$ and MCU$^{\Delta hep}$ mice were lysed in RIPA buffer and probed with indicated antibodies. n= 4 mice. **(L)** Bar graph showing plasma ALTase activity as a measure of liver injury. Mean ± SEM; ns= not

significant; n = 3 mice. **(M)** MCU-KO liver section does not show any gross morphological alterations. Liver from MCU$^{fl/fl}$ and MCU$^{\Delta hep}$ mice were perfused, fixed, and stained with H&E. Representative histological section image (4 x magnification). n = 3 mice per group. **(N)** Loss of MCU in hepatic tissue does not alter the liver triglyceride secretion. **(O)** MCU$^{\Delta hep}$ mice have normal hepatic de novo lipogenesis as measured by palmitate synthesis. Mean ± SEM. ns= non-significant p value; n = 10 mice per group. **(P)** MCU$^{\Delta hep}$ mice have normal white adipose tissue (WAT) de novo lipogenesis as measured by palmitate synthesis. Mean ± SEM. ns= non-significant p value; n = 10 mice per group.

A

WT MCU$^{+/-}$ MCU$^{-/-}$

TMRM

20 μm

B **S4**

ns
ns

TMRM (arb unit)

2800
2100
1400
700
0

WT MCU$^{+/-}$ MCU$^{-/-}$
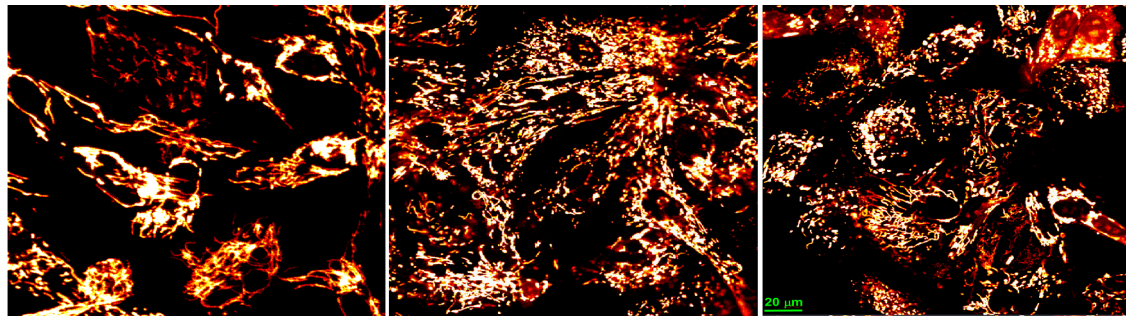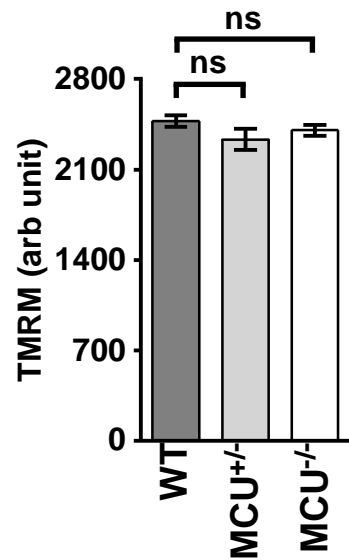
Figure S4 (Related to Figure 3): Assessment of mitochondrial membrane potential ($\Delta\Psi_m$) in zebrafish primary cells.

(A) MCU deletion did not alter $\Delta\Psi_m$. Representative confocal images of primary cells from WT, MCU$^{+/-}$ and MCU$^{-/-}$ zebrafish stained with $\Delta\Psi_m$ indicator, TMRM (50nM). n = 3. **(B)** Quantification of TMRM fluorescence. Mean ± SEM; ns= not significant; n = 3.
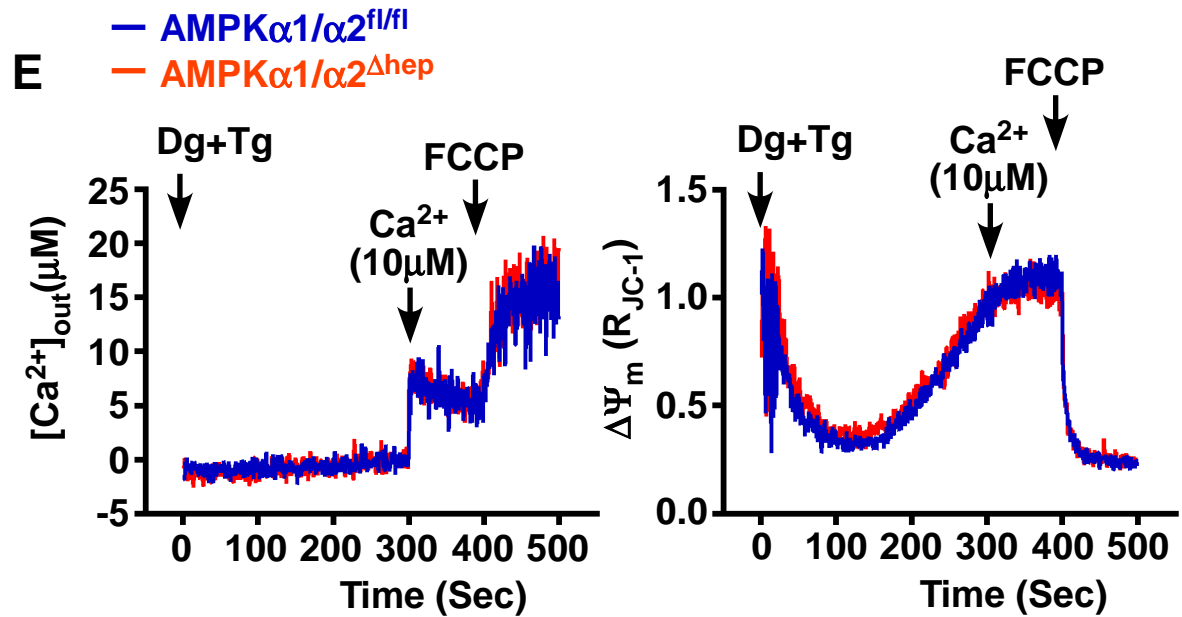
A

Normalized AMPK mRNA Expression

ns

MCU$^{fl/fl}$ MCU$^{\Delta hep}$

B

MCU$^{fl/fl}$ MCU$^{-/-}$

1 2   1 2

pERK

ERK

MCU

βActin

TOM20

C   **S5**

AMPKα1/α2$^{fl/fl}$ AMPKα1/α2$^{\Delta hep}$

BODIPY 493/503

10μm

D

Number of Lipid droplet/Cell

*

AMPKα1/α2$^{fl/fl}$ AMPKα1/α2$^{\Delta hep}$

E

— AMPKα1/α2$^{fl/fl}$
— AMPKα1/α2$^{\Delta hep}$

Dg+Tg

Ca^{2+}
(10μM)

FCCP

$[Ca^{2+}]_{out}$ (μM)

Time (Sec)

Dg+Tg

Ca^{2+}
(10μM)

FCCP

$\Delta\Psi_m$ (R$_{JC-1}$)

Time (Sec)

F

AMPKα1/α2$^{fl/fl}$ AMPKα1/α2$^{\Delta hep}$

TMRM

10μm

G

MCU$^{fl/fl}$ MCU$^{-/-}$

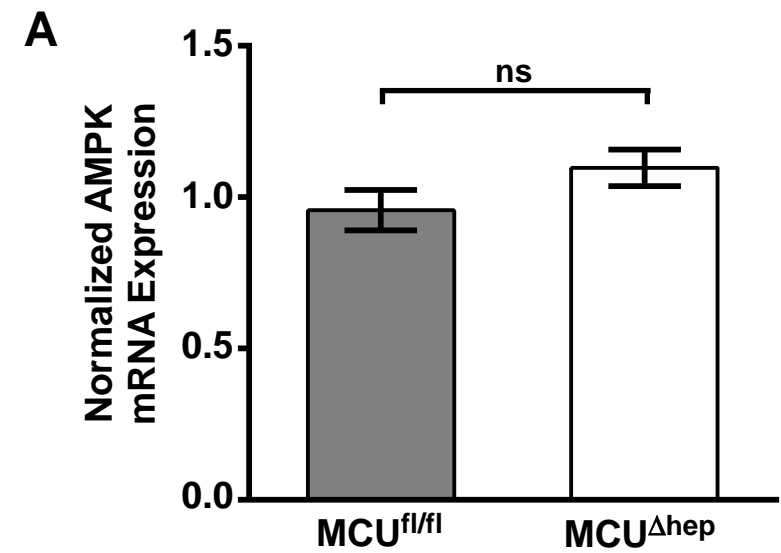Control CA-AMPK Control CA-AMPK

AMPK

βActin

Figure S5 (Related to Figure 4): AMPK mRNA abundance in MCU$^{\Delta hep}$ hepatocytes, ERK-phosphorylation in MCU$^{\Delta hep}$ hepatocytes, BODIPY493/503 staining, Ca^{2+} and $\Delta\Psi_m$ measurement in AMPK $\alpha 1/\alpha 2^{\Delta hep}$ hepatocytes, and reconstitution of CA-AMPK.

(A) AMPK mRNA abundance was quantified in hepatocytes isolated from MCU$^{fl/fl}$ and MCU$^{\Delta hep}$ mice. Mean ± SEM; ns= non- significant p value; n = 4 mice. **(B)** ERK phosphorylation is not suppressed in MCU-KO hepatocytes. Hepatocytes cell lysate prepared from MCU$^{fl/fl}$, MCU$^{\Delta hep}$, and probed with indicated antibodies. n= 4 mice. **(C)** Loss of AMPK$\alpha 1/\alpha 2$ results in the increased lipid droplets in primary hepatocytes. Lipid droplets were visualized by confocal microscopy after BODIPY® 493/503 staining in primary hepatocytes isolated from indicated genotype. n = 3. **(D)** Number of lipid droplets were quantified after BODIPY® 493/503 staining. Mean ± SEM. *p < 0.05; n=20-30 cells. **(E)** Loss of AMPK$\alpha 1/\alpha 2$ does not alter $_m$Ca^{2+} uptake and mitochondrial membrane potential. Representative traces of [Ca^{2+}]$_{out}$ clearance and $\Delta\Psi_m$ in hepatocytes from indicated genotypes. n = 3. **(F)** Hepatic deletion of AMPK$\alpha 1/\alpha 2$ does not affect $\Delta\Psi_m$. Representative confocal images of primary hepatocytes isolated from AMPK$\alpha 1/\alpha 2^{fl/fl}$ and AMPK$\alpha 1/\alpha 2^{\Delta hep}$ mice stained with $\Delta\Psi_m$ indicator, TMRM (50nM). n = 3 mice. **(G)** Primary hepatocytes isolated from MCU$^{fl/fl}$ and MCU$^{\Delta hep}$ mice were infected with control vector and CA-AMPK expressing adeno-virus. Cell lysate prepared and probed with AMPK antibody.
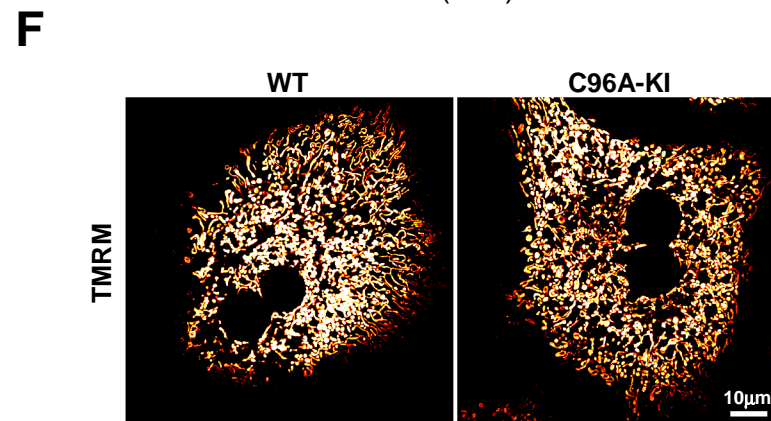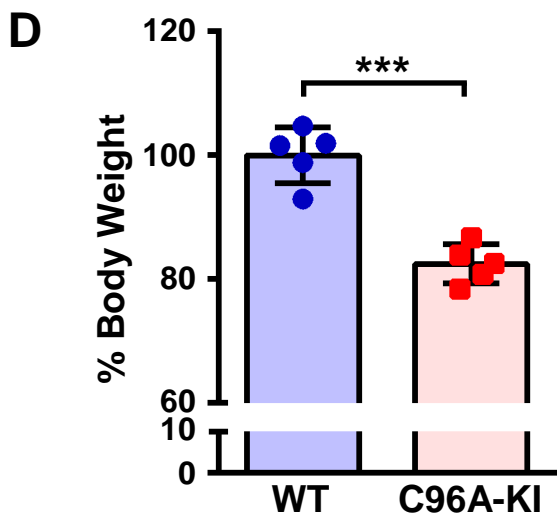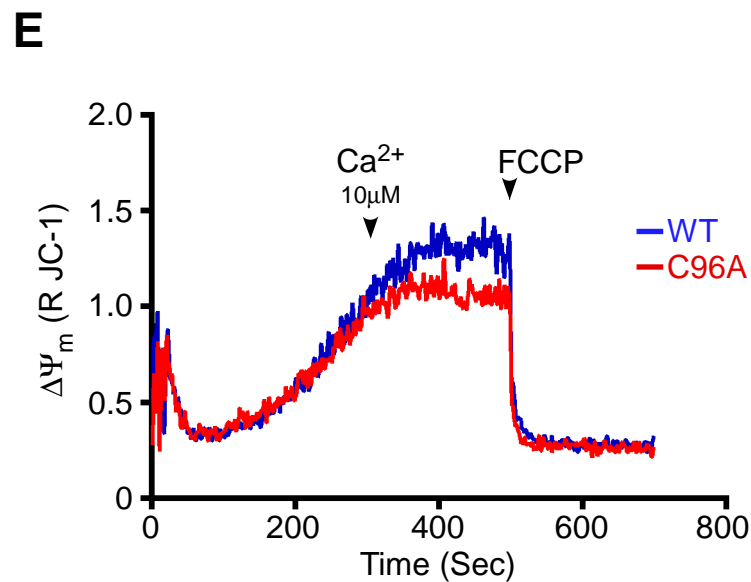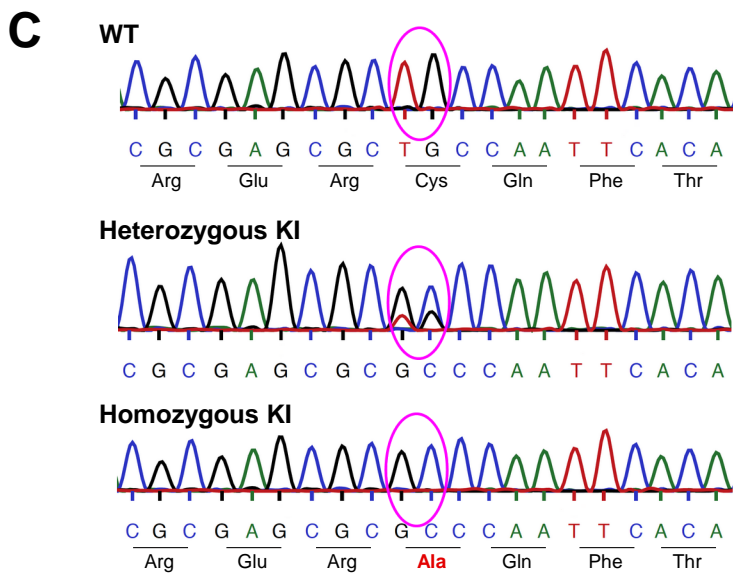
A

WT · C96A · Ca²⁺ · IMS · MCU · Matrix · C96A

B

target gRNA-1 · PAM

WT
5'..ACCCTCTCGACGCGAGCGCTGCCAATTC...TCAAGCCTATCTCTGACTCAGTCGGCGT..3'

3'..TGGGAGAGCTGCGCTCGCGACGGTTAAG...AGTTCGGATAGAGACTGAGTCAGCCGCA..5'

PAM · target gRNA-2

ssODN 5'..CTACCCTCTCGACGCGAGCGCGCCCAATTCACACTCAAGCCTATCTCTGA..3'

BssHII site

C

WT

C G C G A G C G C T G C C A A T T C A C A
Arg · Glu · Arg · Cys · Gln · Phe · Thr

Heterozygous KI

C G C G A G C G C G C C C A A T T C A C A

Homozygous KI

C G C G A G C G C G C C C A A T T C A C A
Arg · Glu · Arg · Ala · Gln · Phe · Thr

D

% Body Weight — WT vs C96A-KI — ***

E

$\Delta\Psi_m$ (R JC-1) vs Time (Sec)

Ca²⁺ 10μM · FCCP · WT · C96A

F

TMRM — WT · C96A-KI · 10μm

Figure S6 (Related to Figure 6): Generation and validation of MCU-C96A KI mice and assessment of $\Delta\Psi_m$.

(A) Schematic represents the constitutive activation of MCU channel due to C96A mutation. **(B)** CRISPR/Cas9 (Nickase) mediated targeting of MCU- genomic region. **(C)** Sequencing data from the WT, heterozygous C96A-KI and homozygous C96A-KI animal shows the replacement of TGC (encode Cys) to GCC (encode Ala). **(D)** The relative body weight of WT and C96A-KI mice. Mean ± SEM. ***p < 0.001, n = 5. **(E)** MCU C96A KI does not affect the $\Delta\Psi_m$. WT and C96A-KI mice hepatocytes were isolated, permeabilized with digitonin (40 μg/mL) in intracellular like media containing thapsigargin (2 μM). The $\Delta\Psi_m$ indicator JC-1 was added at 20 seconds and after reaching steady state $\Delta\Psi_m$. A bolus of extramitochondrial Ca^{2+} (10 μM) was added at the indicated time point before adding the mitochondrial uncoupler FCCP (2 μM). Representative traces of JC-1 staining showing the $\Delta\Psi$m in permeabilized hepatocytes from WT and C96A-KI. n = 3. **(F)** C96A-KI does not affect $\Delta\Psi_m$. Representative confocal images of primary hepatocytes from WT and C96A-KI mice loaded with $\Delta\Psi_m$ indicator, TMRM (50nM). n = 3.
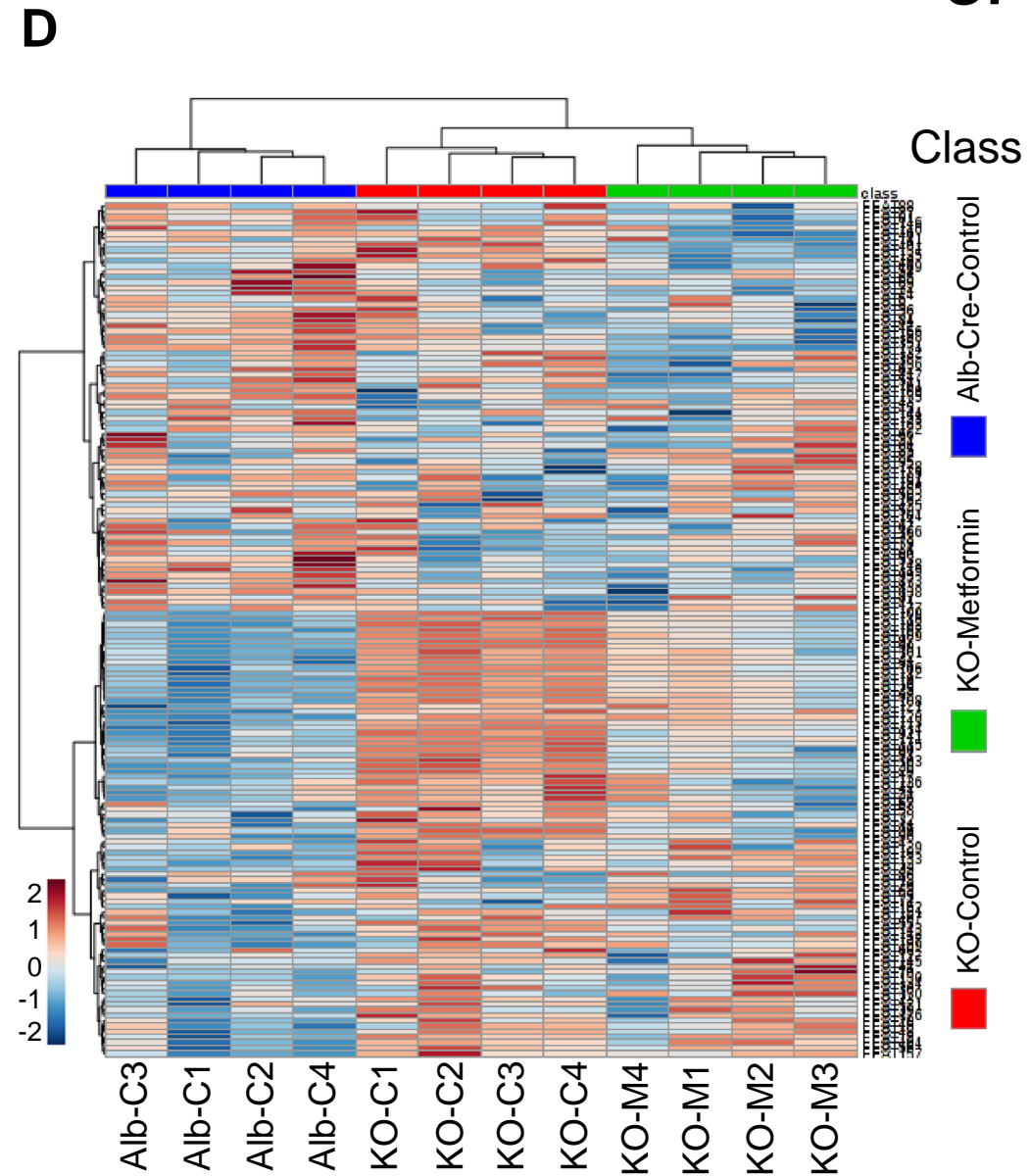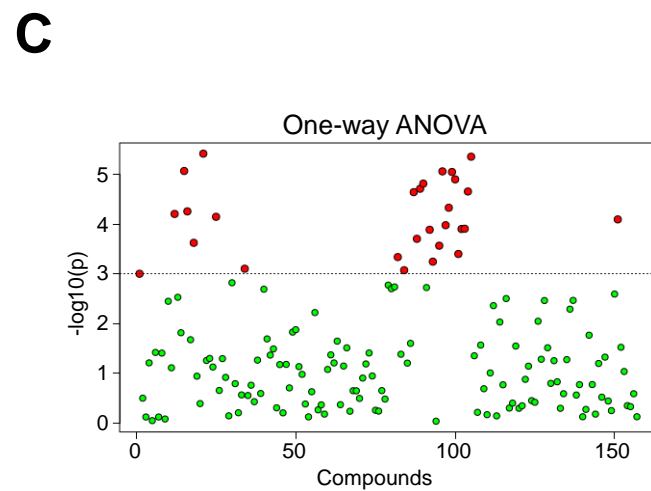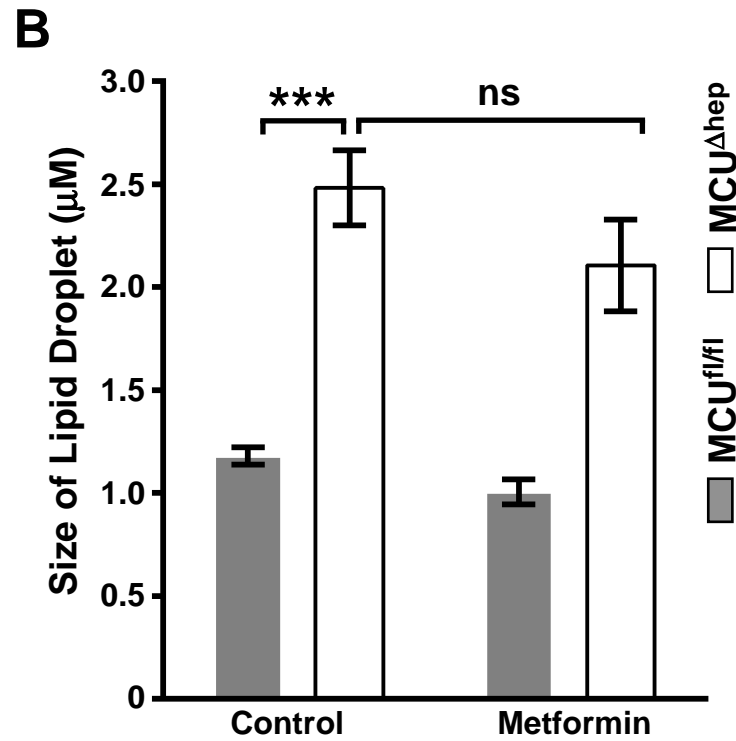
A Hepatocytes

B

C One-way ANOVA

D Class
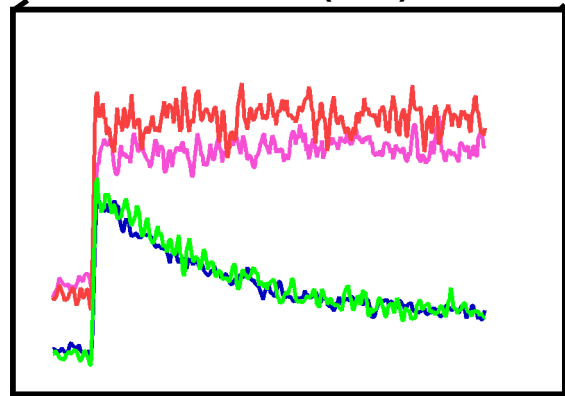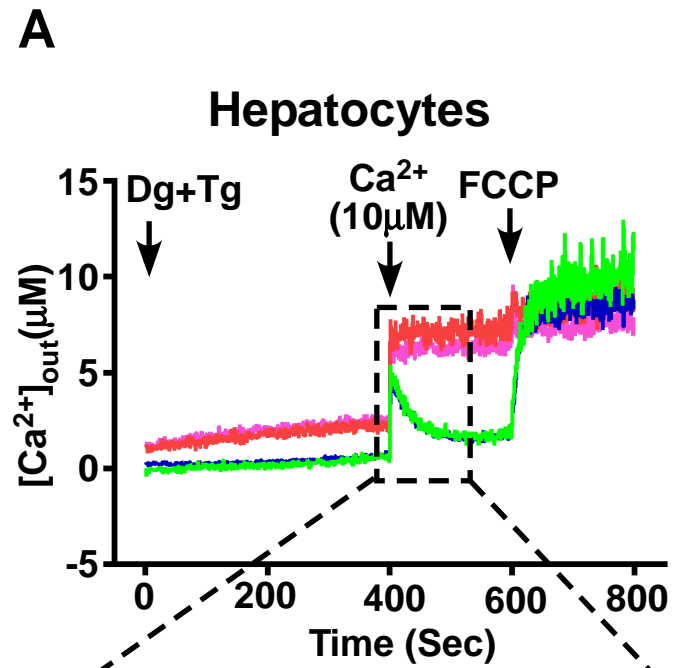
Figure S7 (Related to Figure 7): Effect of metformin on mitochondrial Ca^{2+} uptake and Liver lipidomic alterations in MCU$^{\Delta hep}$ mice.

(A) Metformin treatment did not alter $_m$Ca^{2+} uptake in hepatocytes. Hepatocytes isolated from control and metformin administered MCU$^{fl/fl}$ and MCU$^{\Delta hep}$ mice were isolated, permeabilized with digitonin (40 μg/mL) in intracellular like media containing thapsigargin (2 μM), and bathed in the Ca^{2+} indicator Fura2FF (1 μM). After reaching steady state, a bolus of extramitochondrial Ca^{2+} (10 μM) was added at the indicated time point before adding the mitochondrial uncoupler FCCP (2 μM). Representative traces of [Ca^{2+}]$_{out}$ clearance in permeabilized hepatocytes. n=3. **(B)** Metformin administration does not affect the size of the lipid droplets in MCU-KO hepatocytes. Lipid droplets size were quantified after BODIPY® 493/503 staining. Mean ± SEM. ***$p < 0.001$; ns= not significant; n=15-30 cells. **(C)** A one-way ANOVA was performed on the log transformed extracted features obtained from the untargeted analysis of the lipid extract. Those features identified as being significantly different are represented in red while those features which are not significant are represented in green. n=4 mice per group. **(D)** LCMS features extracted from the LCMS analysis of the lipids were subjected to cluster analysis as described in materials and methods. The data reveal a clear separation in the lipidome between control (Alb-Cre-Control), MCU$^{\Delta hep}$ (KO-Control) and metformin treated MCU$^{\Delta hep}$ mice (KO-Metformin). n=4 mice per group.